Search for a neutral Higgs boson with WH/ZH, H $\to \gamma\gamma$ channel with the CMS detector at the LHC

M. Lethuillier, O. Ravat, J.-L. Agram, C. Baty, S. Gascon-Shotkin, S. Perriès

Available on CMS information server

CMS NOTE 2006/110

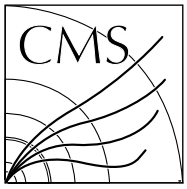

The Compact Muon Solenoid Experiment

CMS Note

Mailing address: CMS CERN, CH-1211 GENEVA 23, Switzerland

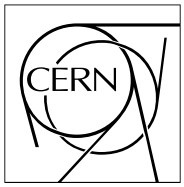

18 January 2007

Search for a neutral Higgs boson with WH / ZH, H$\rightarrow \gamma\gamma$ channel with the CMS detector at the LHC

M. Lethuillier, O. Ravat, J.-L. Agram, C. Baty, S. Gascon-Shotkin, S. Perriès

Institut de Physique Nucléaire de Lyon, CNRS-IN2P3, Université Lyon 1, F69622 Villeurbanne

Abstract

A prospective analysis for the discovery of a light Higgs boson in the Compact Muon Solenoid (CMS) experiment at the Large Hadron Collider (LHC) is presented. The associated production channels WH and ZH of a Higgs boson decaying into a photon pair are studied using a full detector simulation. The method of analysis here employed should permit the utilisation of real data once they become available in order to optimise the analysis performance and to estimate background rates. Minimising in this way reliance on simulated data should allow a significant reduction in systematic errors. One year of LHC running at high luminosity (integrated luminosity of $100\ \mathrm{fb}^{-1}$) should allow an observation at 3σ of the Standard Model Higgs boson from the LEP lower limit of $114.4\ \mathrm{GeV}/c^2$ up to $146\ \mathrm{GeV}/c^2$. Three years of running at high luminosity should allow a 5σ discovery from the LEP lower limit up to $148\ \mathrm{GeV}/c^2$. In the context of supersymmetric models, the dominant gluon fusion Higgs boson production process could be strongly suppressed. This light Higgs gluophobic scenario could occur when the mixing in the stop sector is maximal. In such a case, the associated production channels WH and ZH may be recovery channels.

1 Introduction

The Compact Muon Solenoid (CMS) experiment [1] is a general purpose detector which will operate at the 14 TeV center-of-mass energy proton-proton collider, LHC, at CERN. A main goal of the experiment is the discovery of the Higgs boson. Electroweak precision measurements [2] favour a light Higgs boson ($m_{\mathrm{H}} < 166\ \mathrm{GeV}/c^2$ at 95% CL). In addition, supersymmetric extensions of the Standard Model (SM) also predict that the mass of the lightest neutral scalar Higgs boson h^0 should be limited to approximately $130\ \mathrm{GeV}/c^2$ [3]. Direct searches at LEP have yielded a lower limit at the 95% CL of $114.4\ \mathrm{GeV}/c^2$ for the SM Higgs boson [4] and in the vicinity of $93\ \mathrm{GeV}/c^2$ for the lightest neutral scalar Higgs boson in the CP conserving Minimal Supersymmetric extension of the Standard Model (MSSM) [5]. In this mass range, a favourable discovery channel is its decay into two photons. Compared to the gluon-gluon fusion channel $\mathrm{gg} \rightarrow \mathrm{H} \rightarrow \gamma\gamma$ [6], the associated production channels WH/ZH are expected to suffer from a much lower production cross section. Several advantages, however, make these channels attractive when the decay of the gauge boson results in a charged lepton: requiring an additional relatively high transverse-momentum lepton greatly reduces the significant QCD background in the $\gamma\gamma$ topology and improves the primary vertex reconstruction [7]. In the context of supersymmetric models, maximal mixing in the stop sector could result in a strong suppression of the $\mathrm{gg} \rightarrow \mathrm{h}$ signal process, which the associated production channels would not be subject to [8]. The searched-for final state comprised of 2 isolated photons and at least one isolated electron or muon is close to that of the other associated production channel $\mathrm{t\bar{t}H}$ [9]. The 2-photon signature of a Higgs boson decay has also been studied in association with two forward jets [10]. After one year of high luminosity running, from 88 to 25 events $\mathrm{WH} \rightarrow l\nu\gamma\gamma$ (with $l = e$ or μ) and from 15 to 4 events $\mathrm{ZH} \rightarrow ll\gamma\gamma$ (with $l = e$ or μ) are expected for Higgs boson masses in the range $115 - 150\ \mathrm{GeV}/c^2$. Prior generator-level studies in the context of the Standard Model [11] and of the MSSM [12] showed the possibility of a discovery in this channel. This was confirmed by two ATLAS studies, using a fast simulation, published in [13, 14]. The results presented here are the continuation of the work documented in [15].

2 Event generation and preselection

All the processes considered in this study are simulated at leading order. Signal events are generated by the matrix element generator COMPHEP [16] for Higgs boson masses ranging from 90 to 150 GeV/c^2, in steps of 5 GeV/c^2. At each mass value, 10000 events are generated. Leading order total cross-sections are rescaled according to the next-to-leading order (NLO) calculation [17], via application of K-factors ranging from 1.15 to 1.16 over the whole mass range. Branching ratios for $\mathrm{H} \rightarrow \gamma\gamma$ are taken from the HDECAY program [18]. The irreducible backgrounds from the $\mathrm{W}\gamma\gamma$ and $\mathrm{Z}\gamma\gamma$ processes are also generated with COMPHEP, with the same K-factors applied as those pertinent to the signal process. Fragmentation and hadronization are performed by PYTHIA [19].

The following five most significant reducible background processes are retained due to their capacity to mimic the $l\gamma\gamma$ signal process:

- γ-jet production: one prompt photon, one lepton misidentified within a jet or one lepton from a semi-leptonic decay of a B meson, and the other photon either radiated by the outgoing quark, or coming from a π^0 (or η, ω) decay within a jet;

- $\gamma\gamma$ prompt diphoton production from gluon fusion or quark annihilation: the lepton is either misidentified within a jet or is a B semi-leptonic decay product from a jet radiated in the initial state;

- $\mathrm{W}\gamma$ production: one prompt photon, one lepton coming from the W decay product, and the other photon either radiated by the lepton or misidentified or coming from a π^0 (or η, ω) decay within a jet radiated by one of the initial quarks;

- $\mathrm{t\bar{t}}$ pair production: one lepton from a leptonic decay of a W, and the two photons are either bremsstrahlung emitted by a top, or radiated by the lepton, or coming from a π^0 (or η, ω) decay within a jet, or an electron coming from the other W or from a semileptonic decay of B meson and of whose track was not assigned to the calorimeter cluster;

- $\mathrm{b\bar{b}}$ pair production: the lepton arises from one semileptonic decay, one photon may be radiated by this lepton, and most probably the two photons are mimicked by neutral hadrons within jets. The probability to obtain two isolated photons is much smaller compared to other background processes, but is largely compensated by the very high cross-section.

All these background processes are generated with PYTHIA, and leading order cross-sections are considered, except for the $\mathrm{t\bar{t}}$ production where a NLO cross section of 840 pb is used [20].

To ensure an efficient generation and preserve sufficient statistics of the most signal-like events, a preselection is applied at the generator level. Three electromagnetic candidates, or two electromagnetic candidates and one muon candidate with $E_T > 20$ GeV and $|\eta| < 2.7$ are required [1)]. For background processes generated with PYTHIA, an electromagnetic candidate is obtained by clustering electrons and photons in $\Delta\eta = 0.09, \Delta\phi = 0.09$ window. Muon candidates are either μ, τ, π, or K particles. The cross-sections, the number of generated and preselected events and the statistical weight for each reducible background process are given in Table 1 as an equivalent luminosity in fb^{-1}. For background processes generated with COMPHEP, the electromagnetic and muon candidates are simply the photons and the electron or muon from the hard process. The selection at this level is necessary to avoid divergence problems in COMPHEP.

Table 1: Event preselection at generator level for the 5 most significant reducible background processes, described in the text.

	$\hat{p}_T$ bin (GeV/c)	Cross-section (pb)	Number of generated events	Number of preselected events	Equivalent luminosity (fb^{-1})
$\gamma\gamma$	30-100	107.8	$6.4\ 10^7$	139 500	597
$\gamma\gamma$	> 100	1.95	$5.9\ 10^6$	109 500	3 008
$\mathrm{W}\gamma$	30-100	5.54	$2.0\ 10^7$	80 000	3 683
$\mathrm{W}\gamma$	> 100	0.25	$1.1\ 10^6$	20 000	4 181
$\mathrm{b\bar{b}}$	30-100	$1.8\ 10^6$	$4.6\ 10^8$	25 323	0.26
$\mathrm{b\bar{b}}$	> 100	$1.3\ 10^4$	$5.2\ 10^6$	80 000	0.40
$\mathrm{t\bar{t}}$	–	86.2	$1.2\ 10^6$	80 000	13.3
γ-jet	30-100	$1.2\ 10^5$	$1.7\ 10^7$	5 726	0.14
γ-jet	> 100	$1.8\ 10^3$	$4.4\ 10^6$	79 873	2.52

3 Event reconstruction

The events are generated assuming a pile-up rate corresponding to the planned high luminosity phase of LHC running ($\mathcal{L} = 10^{34}\ \mathrm{cm}^{-2}\mathrm{s}^{-1}$). Full detector simulation and reconstruction is used, based on GEANT 3 [21].

4 Trigger selection

The default trigger tables at high luminosity are used. Events are required to pass the global Level 1 trigger [22]. Only the double photon stream of the High Level Trigger (HLT) which requires asymmetric transverse energies of at least 35 and 20 GeV/c, is selected [23]. These thresholds were optimized for the discovery of the Standard Model Higgs boson produced in the gluon fusion channel and decaying into two photons. The trigger efficiencies for the preselected signal events are higher than 95% for the whole Higgs boson mass range (90 to 150 GeV/c^2). The efficiencies reach 98% for signal events preselected with three electromagnetic candidates and 92% for those preselected with two electromagnetic candidates and one muon candidate. The number of events passing the trigger selection is given in Table 3 for signal and irreducible background processes and in Table 4 for reducible background processes.

5 Offline event selection

5.1 Analysis method

The goal of the first part of the analysis is to eliminate the maximum possible number of reducible background events with large statistical weight (especially $\mathrm{b\bar{b}}$ and γ-jet background processes).

A very loose preselection is applied: at least two offline photons and one electron or muon has to be reconstructed by the standard algorithms. The expected rates of signal and background events at this level are given in Table 2. At this point the expected dominant background processes are from the $\mathrm{b\bar{b}}$ and γ-jet processes.

[1)] In what follows, η is the rapidity defined as $\eta = -\ln(\tan(\frac{\theta}{2}))$ where θ is the polar angle and ϕ the azimuthal angle of a spherical coordinate system, and E_T is the transverse energy defined as $E_T = E\ \sin\theta$.

Four discriminant combined variables (as discussed in the following sections) are then constructed using a likelihood ratio method to estimate:

- y_1, the isolation of the photons
- y_2, the quality of the lepton reconstruction
- y_3, the isolation of the lepton
- y_4, the QCD / multi-jets nature of the event

For each observable x_i, the likelihood ratio $\mathcal{L}_i(x_i)$ is defined as:

$$\mathcal{L}_i(x_i) = \frac{f^S(x_i)}{f^B(x_i)} \tag{1}$$

where f^S and f^B are the probability density functions for the signal and the background. A global discriminant variable y is then constructed as the product of the individual likelihood ratios $\mathcal{L}_i(x_i)$. Theoretically, the combination of several discriminant variables is optimal only if multidimensional functions are used in the likelihood ratio. Nevertheless, with weakly correlated variables, we can make the following approximation:

$$y = \frac{f^S(x_1,\ldots,x_n)}{f^B(x_1,\ldots,x_n)} \simeq \frac{f^S(x_1)\times\ldots\times f^S(x_n)}{f^B(x_1)\times\ldots\times f^B(x_n)} = \prod_{i=1}^{n}\mathcal{L}_i(x_i) \tag{2}$$

Another approach is to apply weights to the individual likelihood ratios to take into account the correlations [24]. To search for the best performance, the curves giving the signal efficiency versus the expected background (obtained by varying the cut on y) are compared for different combinations of variables, retaining those which yield the best rejection accompanied by high signal efficiency ($90-95\%$).

The reference histograms of the input variables used to calculate the four likelihood global variables are all produced from independent simulated event samples at this same level of preselection. These input reference histograms are not produced consecutively (*i.e.* not produced with the subset of events selected by the cut on the previous likelihood), in order to limit the integrated luminosity necessary for an optimization of the likelihood based on real data taken from the $m_{\gamma\gamma}$ sidebands, as will be shown in section 6.1.

Sequential cuts are then applied on these 4 discriminant variables. After the strong suppression of multi-jet background processes ($\mathrm{b\bar{b}}$, $\mathrm{t\bar{t}}$ and γ-jet), some kinematical variables (lepton/photon angles and momentum, magnitude and direction of the missing transverse energy) can be used and combined into a final likelihood variable y_5 to discriminate against more signal-like background processes ($\mathrm{W}\gamma\gamma$, $\mathrm{Z}\gamma\gamma$, $\gamma\gamma$, $\mathrm{W}\gamma$). No kinematical variable is used in the 4 first likelihood variables to avoid correlations between these kinematical variables and the di-photon mass, since this would degrade the performance of the likelihood optimization in the $m_{\gamma\gamma}$ sidebands.

5.2 Photon reconstruction and isolation

Photons are reconstructed with the standard CMS offline algorithms [25]. Photon candidates with a matching seed in the pixel detector are rejected. The two photons with the highest transverse energy are selected. The photon candidates identified in multijet background events come largely from neutral hadrons (π^0, η, ω) within the jets. Photons produced in the decays of these hadrons are strongly collinear with the jet direction. Therefore electromagnetic and hadron calorimeter isolation should permit strong discrimination between these hadron-decay photons and prompt isolated signal photons. Detailed studies of the photon isolation criteria have been previously carried out for the $\mathrm{H}\rightarrow\gamma\gamma$ inclusive analysis [26, 27]. Several variables which estimate the calorimetric energy in the neighbourhood of a photon were tested:

Table 2: Cross-section times branching ratio times selection efficiency after the loose preselection applied before the four likelihood calculations. The preselection requires two offline photons and one offline electron or muon.

	Signals		Backgrounds						
	WH	ZH	$\mathrm{W}\gamma\gamma$	$\mathrm{Z}\gamma\gamma$	$\gamma\gamma$	$\mathrm{W}\gamma$	$\mathrm{b\bar{b}}$	$\mathrm{t\bar{t}}$	γ-jet
$\sigma\times\mathrm{BR}\times\epsilon$ (fb)	0.373	0.040	7.038	7.681	56.9	13.6	63524	1714	21495

- ECAL SimpleCone: Sum of the transverse energy of the fundamental component clusters (reconstructed with the "island" algorithm [28]) within a cone $\Delta R < 0.3$ around the photon, where $\Delta R = \sqrt{(\Delta\eta^2 + \Delta\phi^2)}$, excluding the fundamental component clusters belonging to the photon supercluster (see Figure 1);
- ECAL BiCone: Sum of the transverse energy of the island fundamental component clusters within a double cone $0.08 < \Delta R < 0.3$ centred on the reconstructed photon (see Figure 2);
- SCISO: Sum of the transverse energy of the island fundamental component clusters within a double cone $0.08 < \Delta R < 0.35$ centred on the reconstructed photon, excluding the fundamental component clusters in a $|\Delta\eta| < 0.03$ band (see Figure 3). This isolation variable is similar to the one used by default for electromagnetic objects in the CMS standard reconstruction program ORCA [29]. The Phi ring is used to exclude from the isolation method the clusters due to bremsstrahlung;
- HCAL Iso: Sum of the transverse energy of the HCAL towers within a cone $\Delta R < 0.3$ around the reconstructed photon (see Figure 4);
- HCAL nTowers: Number of HCAL towers hit withinin a cone $\Delta R < 0.3$ around the reconstructed photon (see Figure 5).

The use of isolation criteria involving the pixel detector was also considered. This enables slightly increased discrimination power but at the price of a non-negligible loss in signal efficiency. Since the goal is to preserve the highest efficiency possible before entering the second part of the analysis (use of kinematical variables), these additional criteria were not adopted.

The best performance is obtained with the combination of the ECAL SimpleCone and the HCAL Iso variables for both photons using the method described in section 5.1. The distribution of the resulting discriminant variable y_1 is shown in Figure 6. We apply the criterion $log(y_1) > -0.4$, which is particularly effective against $\mathrm{b\overline{b}}$ pair production (rejection factor of 76) as well as against top quark pair production (rejection factor of 30). On the other hand, the γ-jet background process is only reduced by a factor of 4 by this cut on y_1 due to the presence of a genuine isolated photon.

5.3 Quality of the lepton reconstruction

The standard offline algorithms are used to reconstruct the electrons [30] and the muons [31]. Sometimes several tracks correspond to the same reconstructed electron cluster; the track with the momentum closest to the cluster energy is then chosen. The lepton candidate is then defined as the electron or muon with respectively the highest E_T measured by the electromagnetic calorimeter, or p_T. We then seek to verify good reconstruction quality for the lepton candidate and to reject misidentified leptons produced within jets. In the case of multijet events, the density of particles within a jet is such that the calorimetric deposits from photons or neutral hadrons are frequently erroneously associated with a track and are wrongly identified as electrons.

Numerous variables involving the calorimetry and the tracker system were tested. The four variables yielding the most significant discriminating power are:

- $\mathrm{E_{em}}$/p: the ratio between the electron energy as measured in the electromagnetic calorimeter and its momentum measured by the tracker. This ratio should tend towards 1 when the calorimetric deposit has been correctly associated to a track. The distribution of this variable is shown in Figure 7;
- $\mathrm{E_{had}}$/E: the hadronic energy fraction given by the ratio between the energy measured in the hadron calorimeter and the sum of the energies measured in the electromagnetic and hadron calorimeters;
- $\Delta\eta$ trk-clus: The difference in η between the track and the associated supercluster. This value should tend towards 0 in the case of a correct association. The angle in phi is not considered, due to bremsstrahlung. Under the influence of the magnetic field, the electron tends to distance itself in phi from the radiated photons. The distribution of this variable is shown in Figure 8;
- r9: The ratio between the sum of the energies of 9 crystals (3x3 matrix centred on the maximum-energy crystal) and the energy of the corresponding supercluster. This ratio is related to the shower shape. Electrons having experienced little bremsstrahlung have their energy concentrated in the shower center (see Figure 9).

The above four variables are combined in a likelihood variable y_2, as explained in section 5.1. The distribution of the output variable y_2 is shown in Figure 10. A cut $log(y_2) > -0.6$ is applied.

In the case of muons, the purity obtained by the standard CMS reconstruction algorithms is such that no additional criteria need be applied (the measured false rate at which the pion tracks within bottom quark jets are globally reconstructed as muons is 0.17 % [32]).

5.4 Lepton isolation

In most of the reducible background processes, the identified lepton candidate is misidentified within a jet or is a B semi-leptonic decay product, far less isolated than a lepton coming from a W or Z decay. The same variables as those studied for photons are tested. For the electron, the method is quite similar to the photon case. For muons, the muon track is extrapolated through the magnetic field to the calorimeter. The only difference is that no cluster is associated with the muon, so no basic clusters are removed during the calculation of the ECAL SimpleCone variable, and the energy deposited by the muon in the calorimeter is not subtracted. That is why the ECAL BiCone variable offers better performance than the SimpleCone one. The best combination is obtained with the ECAL BiCone and the HCAL Iso variables. The distributions are presented in Figures 11 and 12. In addition, the number $\mathrm{N_{pxl}}$ of pixel lines within a cone $\Delta R < 0.3$, presented in Figure 13, improves the discriminative power of the likelihood. The global likelihood variable y_3 is formed by the combination of the three variables ECAL BiCone, HCAL Iso and $\mathrm{N_{pxl}}$, using the method described in section 5.1.

In the future, some performance improvement of the lepton isolation is expected by using the full tracker information as was done in [24]. The distribution of the likelihood variable y_3 is shown in Figure 14. A cut $log(y_3) > -0.3$ is applied.

5.5 Multi-jet events rejection

The rejection of photons from π^0 decays in QCD background processes, which could be misidentified as Higgs boson decay photons, has been accomplished by a neural net procedure exploiting the information on the lateral profile of the electromagnetic shower. The distributions of the discriminant variable for the two photon candidates are shown in Figures 15 and 16.

Variables involving the multiplicity of reconstructed objects in the electromagnetic calorimeter reinforce the discriminating power, in particular, the number of seed clusters reconstructed by the island algorithm, as shown in Figure 17. The global variable y_4 is obtained by the likelihood ratio method described in section 5.1 combining the two anti-π^0 neural net variables associated to the two photon candidates and the number of electromagnetic seed clusters.

The distribution of the combined variable y_4 is given in Figure 18. A cut $log(y_4) > -0.8$ is applied on this variable.

Table 3: Production cross-section times branching ratio, and cross-section times branching ratio times preselection efficiency after each stage of the event selection, for signal processes ($m_{\mathrm{H}} = 120\ \mathrm{GeV}/c^2$) and irreducible background processes. All values are shown in fb. Errors are statistical only.

	Signals		Irreducible backgrounds	
	WH	ZH	W$\gamma\gamma$	Z$\gamma\gamma$
$\sigma \times \mathrm{BR}$	0.810	0.137	-	-
Preselection: $\sigma \times \mathrm{BR} \times \epsilon$	0.460	0.0440	13.58	18.92
Double photons HLT	0.439 ± 0.005	0.0423 ± 0.0004	8.80 ± 0.04	12.13 ± 0.07
At least 2 offline photons	0.415 ± 0.005	0.0400 ± 0.0004	8.23 ± 0.04	10.01 ± 0.06
$E_T(\gamma 1) > 35$ GeV	0.411 ± 0.005	0.0394 ± 0.0004	7.47 ± 0.04	7.30 ± 0.05
Photons isolation	0.387 ± 0.005	0.0370 ± 0.0004	7.14 ± 0.04	6.51 ± 0.04
At least 1 offline lepton	0.348 ± 0.004	0.0362 ± 0.0003	5.94 ± 0.04	4.80 ± 0.03
Lepton quality	0.331 ± 0.004	0.0350 ± 0.0003	5.56 ± 0.04	4.58 ± 0.03
Lepton isolation	0.299 ± 0.004	0.0318 ± 0.0003	4.83 ± 0.04	4.11 ± 0.03
QCD rejection	0.281 ± 0.004	0.0273 ± 0.0003	4.50 ± 0.04	3.53 ± 0.03
$\Delta R(\gamma\gamma l) > 0.3$	0.281 ± 0.004	0.0272 ± 0.0003	4.49 ± 0.04	3.52 ± 0.03
$80 < m_{\gamma\gamma} < 160$	0.271 ± 0.004	0.0259 ± 0.0003	2.04 ± 0.02	1.42 ± 0.02

Table 4: Production cross-section times branching ratio, and cross-section times branching ratio times preselection efficiency after each stage of the event selection, for reducible background processes. Contributions of the different $\hat{p}_T$ bins are summed. All values are shown in fb. Errors are statistical only.

	Reducible backgrounds				
	$\gamma\gamma$	$\mathrm{W}\gamma$	$\mathrm{b\bar{b}}$	$\mathrm{t\bar{t}}$	γ-jet (jet)
$\sigma \times \mathrm{BR}$	1.1×10^5	5.79×10^3	1.78×10^9	86.2×10^3	1.21×10^8
Preselection: $\sigma \times \mathrm{BR} \times \epsilon$	270.1	26.5	2.96×10^5	6.00×10^3	7.16×10^4
Double photons HLT	197.7 ± 1.0	16.8 ± 0.1	77120 ± 764	1948 ± 17	35045 ± 256
At least 2 offline photons	194.4 ± 1.0	15.2 ± 0.1	71935 ± 738	1872 ± 17	32038 ± 244
$E_T(\gamma 1) > 35$ GeV	187.0 ± 0.9	13.6 ± 0.09	51991 ± 627	1069 ± 13	31098 ± 241
Photons isolation	161.6 ± 0.8	9.97 ± 0.07	682 ± 72	31.2 ± 2.2	7235 ± 115
At least 1 offline lepton	39.1 ± 0.4	8.52 ± 0.07	523 ± 63	27.0 ± 2.0	4751 ± 93
Lepton quality	27.3 ± 0.3	7.98 ± 0.07	311 ± 49	23.5 ± 1.9	2552 ± 68
Lepton isolation	9.8 ± 0.2	6.59 ± 0.06	(0.87)	14.2 ± 1.5	209 ± 20
QCD rejection	7.6 ± 0.2	5.74 ± 0.06	(0.003)	(0.35)	(6.6)
$\Delta R(\gamma\gamma l) > 0.3$	7.6 ± 0.2	5.70 ± 0.06	(0.002)	(0.31)	(5.3)
$80 < m_{\gamma\gamma} < 160$	3.2 ± 0.1	2.40 ± 0.04	(0.001)	(0.26)	(3.7)

5.6 Kinematical selection - Final likelihood variable

The results of the sequential cuts applied to the 4 combined variables are presented in Tables 3 and 4. The multijet background processes are entirely suppressed. The cut factorisation method is applied in order to estimate the contribution of these background processes which are reduced to zero due to finite statistics. In this approach, the photon isolation criteria are temporarily removed in order to estimate the efficiencies of the last cuts (lepton isolation and beyond). These efficiencies are then applied to the number of events remaining before the cuts (which have removed all of them in the present analysis). The estimations obtained by this method are indicated between parentheses in Tables 3 and 4. After rejecting events outside the 80-160 GeV/c^2 di-photon mass window, the expected rate of surviving events is:

WH/ZH, H$\rightarrow \gamma\gamma$ signals: $\sigma \times \mathrm{BR} \times \epsilon = 0.297 \pm 0.004$ fb

All other background processes: $\sigma \times \mathrm{BR} \times \epsilon = 13.1 \pm 2.6$ fb

Some simple kinematical variables are used to form a final likelihood variable y_5. The reference S/B histograms are produced using half of the statistics available after the sequential selection (35990 MC events for signal processes and 10630 MC events for background processes). The more discriminant variables are identified:

- the transverse energy of the photons, represented in Figures 19 and 20;
- the transerve calorimeter energy of the electron or the transverse momentum of the muon, shown in Figure 21;
- the ΔR distances between lepton and each photon, represented in Figures 22 and 23;
- the missing transverse energy (which was calculated using an iterative cone algorithm [33] for jet clustering with a cone size of 0.6 and a $p_T > 15$ GeV/c threshold for the jets), represented in Figure 25;
- the phi angle between the direction of the missing eneregy and the direction of the first photon, represented in Figure 26.

These seven variables are then combined, using the method described in section 5.1, to form the final global variable y_5. The ΔR distance between the two photons (see Figure 24) is also discriminant but is strongly correlated with the di-photon reconstructed mass used to derive the statistical significances, so it is not kept to form the final likelihood. The distribution of the resulting combined variable y_5 is shown in Figure 27 for a Higgs boson mass of 120 GeV/c^2.

5.7 Statistical method and optimization

The statistical methods developed by the LEP Higgs working group [34] are used in this analysis to optimize the selection criteria and evaluate the statistical significance of the expected results. It will never be possible to exclude with an absolute certainty the presence or absence of a signal (In the following, the background-only hypothesis

(the null hypothesis) will be noted b, and $s+b$ will be used for the signal+background hypothesis). Therefore a Confidence Level (CL) is introduced to characterize the statistical significance of the exclusion or discovery of a signal. The first step to obtain this CL is to select the most discriminating observables. These variables are then used to construct the test-statistic X which classifies the experiments according to their more or less background-like or (signal+background)-like nature. The test-statistic will also be used to determine the confidence level to exclude the b or $s+b$ hypothesis.

Test-statistic - the test-statistic is chosen to increase monotonically for more signal-like experiments. The probability of rejecting a false hypothesis at a given confidence level is maximized by using a likelihood ratio as test-statistic:

$$X = \frac{\mathcal{L}_{s+b}}{\mathcal{L}_b}. \tag{3}$$

The most obvious information which has to be included in the likelihood function is the counting rates of the expected signal s and background b events. The s and b rates follow a Poisson probability distribution, and thus:

$$X = \frac{e^{-(s+b)}\,(s+b)^n/n!}{e^{-b}\,b^n/n!}, \tag{4}$$

where n is the number of observed events. The separative power of the likelihood function can be improved by the addition of other discriminating variables such as the reconstructed di-photon mass. If this additional variable x is distributed like $S(x)$ and $B(x)$ for respectively the signal and background events, then the test-statistic is defined by :

$$\begin{aligned} X &= \frac{e^{-(s+b)}\,(s+b)^n/n!}{e^{-b}\,b^n/n!}\;\frac{\prod_{j=1}^{n}\frac{sS(x_j)+bB(x_j)}{s+b}}{\prod_{j=1}^{n}B(x_j)} &(5)\\ &= e^{-s}\prod_{j=1}^{n}\left(1+\frac{sS(x_j)}{bB(x_j)}\right). &(6)\end{aligned}$$

This result is easily extended to the case of a multi-channel search:

$$X = e^{-s_{tot}}\prod_{i=1}^{N}\prod_{j=1}^{n_i}\left(1+\frac{s_i S_i(x_{ij})}{b_i B_i(x_{ij})}\right), \tag{7}$$

where N is the number of channels to be considered, n_i is the number of observed candidates in the channel i, s_i and b_i are the expected signal and background rates for the channel i, s_{tot} is the total expected number of signal events, x_{ij} is the value of the discriminating variable obtained for the candidate j of channel i, S_i and B_i are the probability density functions of the discriminating variable for the signal and the background of the channel i.

Definition of the Confidence Level - The test-statistic X increases monotonically for increasingly signal-like experiments. The CL in the $s+b$ hypothesis can therefore be defined as the probability that a $s+b$ experiment gives a value X of the test-statistic lower than the observed X_{obs} :

$$\mathrm{CL}_{s+b} = \mathcal{P}_{s+b}(X \le X_{obs}) = \int_0^{X_{obs}} \frac{d\mathcal{P}_{s+b}}{dX}dX, \tag{8}$$

where $d\mathcal{P}_{s+b}/dX$ is the probability density function of the test-statistic in the case of signal+background experiments. The confidence level in the null hypothesis is defined by:

$$\mathrm{CL}_b = \mathcal{P}_b(X \leq X_{obs}) = \int_0^{X_{obs}} \frac{d\mathcal{P}_b}{dX} dX. \tag{9}$$

A 5σ discovery will be established when the probability $1 - \mathrm{CL}_b$ that a background-only experiment gives a more signal-like result than the observation is less than 5.7×10^{-7}.

The CL in the signal hypothesis is defined using a modified frequentist renormalization :

$$\mathrm{CL}_s = \mathrm{CL}_{s+b}/\mathrm{CL}_b, \tag{10}$$

and the presence of signal will be said to be excluded at a CL equal to $1 - \mathrm{CL}_s$.

Choice of the working point - To form the test-statistic, the two obvious variables to be used are the reconstructed $\gamma\gamma$ invariant mass and the kinematical likelihood variable y_5. The limited statistics of the MC events prohibit, however, the use of a two-dimensional method for the determination of the Higgs boson discovery potential. Therefore, only the shape of the reconstructed $\gamma\gamma$ mass distribution will be used, along with a cut on the combined likelihood variable y_5. The choice of the optimal working point (i.e. the y_5 cut value) will be that which maximizes the discovery potential. Figure 28 illustrates the optimization process for $m_{\mathrm{H}} = 120\ \mathrm{GeV}/c^2$ and an integrated luminosity of $100\ \mathrm{fb}^{-1}$. For each tentative cut on the global variable y_5, the $m_{\gamma\gamma}$ distribution is drawn for signal and background processes and is used as input for the confidence level calculation. The statistical significance obtained as a function of the cut on y_5 is shown in Figure 29. The cut on y_5 which maximizes the significance is chosen. This optimal working point is a function of the m_{H} hypothesis but is independent of the integrated luminosity, to the extent that systematic uncertainties are not taken into account. The statistical significance can be easily traced as a function of the luminosity as shown in Figure 36 for all m_{H} hypotheses. The list of the optimal working points obtained for the different Higgs boson mass hypotheses is given in Table 5. The significance and the expected number of signal and background events are given for a luminosity of $100\ \mathrm{fb}^{-1}$. For the γ-jet, $\mathrm{t\bar{t}}$ and $\mathrm{b\bar{b}}$ background processes, the rates are estimated by the method of cut factorization described in section 5.6.

Table 5: Optimal working points for the different Higgs boson mass hypotheses. The significance and the expected number of signal and background events are given for an integrated luminosity of $100\ \mathrm{fb}^{-1}$.

			Signals		Irreducible backgrounds		Reducible backgrounds				
m_{H} (GeV/c^2)	working point $log(y_5) >$	significance	WH	ZH	W$\gamma\gamma$	Z$\gamma\gamma$	Wγ	$\gamma\gamma$	γ-jet	$\mathrm{t\bar{t}}$	$\mathrm{b\bar{b}}$
90	0.24	5.66 σ	38.9	3.2	66.2	42.9	51.6	14.7	1.3	0.37	13×10^{-5}
95	0.28	5.18 σ	34.0	2.8	63.8	37.7	48.8	12.3	1.4	0.28	13×10^{-5}
100	0.28	5.27 σ	32.2	2.6	62.6	39.4	48.2	13.4	1.6	0.30	16×10^{-5}
105	0.53	4.92 σ	25.2	2.2	47.2	26.1	32.2	7.4	1.1	0.19	7×10^{-5}
110	0.56	4.73 σ	22.6	2.0	43.0	25.2	28.3	7.6	1.2	0.16	7×10^{-5}
115	0.41	4.30 σ	22.1	1.8	49.3	30.9	33.0	10.2	1.7	0.16	10×10^{-5}
120	0.35	4.09 σ	20.7	1.6	51.2	36.2	34.5	12.4	1.9	0.15	10×10^{-5}
125	0.59	4.01 σ	17.1	1.4	36.3	21.2	23.6	7.0	1.3	0.12	7×10^{-5}
130	0.68	3.64 σ	14.6	1.3	30.7	16.9	18.7	6.0	1.4	0.10	4×10^{-5}
135	0.82	3.47 σ	13.1	1.2	24.9	13.2	15.0	5.0	1.2	0.07	3×10^{-5}
140	0.99	3.35 σ	11.4	1.0	18.9	10.3	10.6	3.7	1.0	0.04	1×10^{-5}
145	1.18	3.13 σ	9.7	0.8	13.8	6.5	7.9	2.9	0.7	0.03	$< 1 \times 10^{-5}$
150	0.83	2.87 σ	10.4	0.9	20.2	11.7	12.3	5.4	1.1	0.03	3×10^{-5}

6 Use of real data in sidebands - Systematic uncertainties

The signal searched for is characterized by a strongly peaked di-photon invariant mass. Furthermore, at the optimal working points, the $m_{\gamma\gamma}$ distribution of the background is smooth and flat. When real data become available, this will allow us to use the data taken in $m_{\gamma\gamma}$ sidebands to optimize the likelihood analysis and to estimate the background rate.

6.1 Likelihood optimization with sideband events

No kinematical observables were used to construct the four primary likelihood variables aimed at rejecting multijet events. If the shapes of the distributions of the variables used in the likelihoods are sufficiently similar for different di-photon mass regions, then data taken outside the signal region can be used to optimize the likelihood. Only the signal MC will be used, and the analysis does not rely on the background MC, avoiding the possibly large related uncertainties. To test the method, a sample of simulated events corresponding to possible future real dataset is used: the number of MC events for each background process is equal to the expected number of events for a given luminosity (*i.e.* the MC events for different processes have all a weight equal to 1). The size of the sample is limited by the equivalent luminosity of the MC samples produced. The same preselection as in the standard analysis is used: two offline photons and one electron or muon are required. The reference S/B histograms for the likelihoods are produced with the events taken in the $20 < m_{\gamma\gamma} < 80$ GeV/c^2 band. The total number of MC events available in this band is given in Table 6. This table also shows that the equivalent integrated luminosity corresponding to the simulated data sample is limited to 132 pb^{-1} by the statistics available for the $\mathrm{b\overline{b}}$ background process. The composition of the sample is given in the last column of Table 6. The dominant contribution of $\mathrm{b\overline{b}}$ events amounts to 87%, γ-jet events represent 9%, and $\mathrm{t\overline{t}}$ events 4%. The reference S/B histograms of the likelihood ratio method are produced with these events, and the four global variables y_1, y_2, y_3, y_4 are then calculated for the events in the $80 < m_{\gamma\gamma} < 160$ GeV/c^2 band. The performance is compared to the results obtained in the same $80 - 160$ GeV/c^2 band by the standard analysis optimized with the full MC statistics available. The distributions of the photon isolation combined variable y_1 are shown in Figure 30 for these two cases, and Figure 31 illustrates the comparison of the performance obtained by the two methods. For the four global discriminant variables, up to 20% loss of efficiency is observed for the same rejection power. The degradation of the performance is mainly due to the insufficient statistics of γ-jet and $\mathrm{t\overline{t}}$ events in 132 pb^{-1} of data: $\sim$200 γ-jet events is clearly insufficient to obtain the full discrimination power of the combined variables against this background process.

To increase the size of the simulated data sample, gedanken experiments are generated: the absence of correlations between the input variables used to form the global likelihood variables is assumed. The distributions of these input variables in the $20 < m_{\gamma\gamma} < 80$ GeV/c^2 kinematical region are then fitted and used to generate the pseudo-experiments. The performance obtained is represented in Figure 31. It is seen that an integrated luminosity of 5 fb^{-1} will be sufficient to optimize the four primary likelihoods with the future real data taken in the $m_{\gamma\gamma}$ sideband and to reproduce the results obtained when using the full MC statistics.

Table 6: Results of the preselection in the $20 < m_{\gamma\gamma} < 80$ GeV/c^2 sideband.

	Nb of selected MC events	$\sigma \times \mathrm{BR} \times \epsilon$ (fb)	Equivalent luminosity (fb^{-1})	Number of events for 132 pb^{-1}
$\mathrm{W}\gamma\gamma$	11772	3.393	3469	0
$\mathrm{Z}\gamma\gamma$	21805	4.126	5285	1
$\gamma\gamma$	3945	18.5	213	2
$\mathrm{W}\gamma$	11375	6.22	1829	1
$\mathrm{b\overline{b}}$	4682	35501	0.132	4682
$\mathrm{t\overline{t}}$	11149	1682	6.63	222
γ-jet	1935	3523	0.549	465

6.2 Background measurement from Data

After the selection by the final likelihood variable at the optimal working points, the $m_{\gamma\gamma}$ distribution of the background is smooth enough to be easily fit. When the real data become available, it will be possible to take a $m_{\gamma\gamma}$ window centred on the m_{H} hypothesis, then fit the real data outside this window to estimate the background within the signal window. If the number of events in the sideband is sufficient, this method can be applied, and will considerably simplify the estimation of the systematic uncertainties on the expected background rate. The MC can be used to optimize the method (size and position of the window, bin width, choice of the fit function, *etc*...) and to estimate the uncertainty on background: the $m_{\gamma\gamma}$ distribution can be used to generate thousands of signal+background pseudo-experiments. The data from these pseudo-experiments are fitted excluding a mass window around the peak as shown in Figure 32. The number N_{bkg}^{fit} of background events in the signal region is given by the integral of the fit function in this mass window. The full statistics MC distribution is fitted over the whole mass range. The number N_{bkg}^{MC} of predicted events in the signal region is the integral of the fit function in the signal mass window. The relative error on the measure is given by the ratio $N_{bkg}^{fit}/N_{bkg}^{MC}$ and is represented in Figure 33 for 10000 pseudo-experiments for a 120 GeV/c^2 Higgs boson mass hypothesis and integrated luminosi-

ties of $100\ \mathrm{fb}^{-1}$ and $300\ \mathrm{fb}^{-1}$. The mean of the Gaussian fit to the $N_{bkg}^{fit}/N_{bkg}^{MC}$ distribution gives the rescaling factor to apply to the background rate. This factor is related to the width of the signal window. A too narrow window increases this scaling factor; the background rate is overestimated due to the signal events in the tail. A too large window will reduce the precision of the fit. 10000 gedanken experiments have been generated for each m_{H} hypothesis at each luminosity point. For all Higgs boson masses, the best results correspond to a symmetric window of $\pm 8\ \mathrm{GeV}/c^2$, a bin width of $4\ \mathrm{GeV}/c^2$ and a second order polynomial background fit function. The relative uncertainty obtained on the background rate estimation is represented as a function of the luminosity in Figure 34 for a Higgs boson mass of $120\ \mathrm{GeV}/c^2$. For a luminosity of $100\ \mathrm{fb}^{-1}$ and a Higgs boson mass of $120\ \mathrm{GeV}/c^2$, the background rate is measured with a precision of 11%, and with a precision of 6.6% for $300\ \mathrm{fb}^{-1}$. The background rate uncertainty for each m_{H} hypothesis can be parametrized by:

$$\frac{\Delta B}{B} = \frac{\alpha(m_{\mathrm{H}})}{\sqrt{\mathcal{L}}} \quad , \quad \text{with } \mathcal{L} \text{ in } \mathrm{fb}^{-1} \tag{11}$$

The inferred $\alpha(m_{\mathrm{H}})$ values are given in Table 7.

Table 7: List of the α parameters used to parametrize the relative uncertainty on the background rate estimated by the sideband fit.

m_{H} (GeV/c^2)	90	100	110	120	130	140	150
$\alpha(m_{\mathrm{H}})$	0.96	0.96	0.95	1.14	1.13	1.83	1.76

6.3 Systematic uncertainties for signal and cross-section measurement

The following sources of error were considered:

- the theoretical cross-section error due to the renormalization and factorization scale variation: the renormalization scale and factorization scale will be identified. To estimate the uncertainty on the theoretical cross-section, this scale is varied between 0.5 and 2 times the central scale value. For the process $\mathrm{V}^* \rightarrow \mathrm{VH}$, the central scale value is given by the invariant VH mass. The error obtained is $\pm 3\%$ for WH and ZH production for all considered Higgs boson masses [17]; it has been checked that no accidental compensation of scale dependences is introduced by identifying renormalization and factorization scales.
- the error on the structure functions of protons: the parton density function (PDF) of the CTEQ collaboration has been used [36]; The PDF uncertainty for the associated production $\mathrm{q\overline{q}} \rightarrow \mathrm{VH}$ at the LHC is almost constant and of the order of 4% over a Higgs boson mass range between 100 and 200 GeV/c^2 [37];
- the error on the measured luminosity: this is expected to be 3% for luminosity above 30 fb^{-1} [38];
- the error on the lepton or photon reconstruction and identification has been estimated to 1% for each identified photon and lepton candidate [39, 40];
- the error on the missing transverse energy: the error amounts to 10% for low p_T jets and unclustered energy, and to 3% for high p_T jets [41]. A value of 5% is used and propagated in the final likelihood. This results in a -1.08% +0.49% variation of the final signal rate for $m_{\mathrm{H}} = 120\ \mathrm{GeV}/c^2$.

The quadratic sum of all these errors gives a 6% total error on the expected signal rate.

6.4 Effect of systematic uncertainties on confidence levels

To propagate the systematic uncertainties in the confidence level calculation, the signal and background expectation values are randomized when computing the probability density functions of the test-statistic as described in [34, 35]. The probability distributions of the systematic uncertainties are assumed to be Gaussian. The systematic uncertainty on the background rate comes from the sideband fit procedure, described in section 6.2, and is equal to 11 % for a $120\ \mathrm{GeV}/c^2$ Higgs boson and an integrated luminosity of $100\ \mathrm{fb}^{-1}$. The signal systematic uncertainty has both theoretical and instrumental origins, as described in section 6.3, and is equal to 6%. There is no observed effect of the signal systematic uncertainty on the confidence level in the case of signal+background experiments and background-only experiments. The total systematic uncertainty is completely dominated by the error on the

background measurement. Figure 36 shows the statistical significance as a function of the integrated luminosity of the LHC running at high luminosity ($\mathcal{L} = 10^{34}\ \mathrm{cm}^{-2}\mathrm{s}^{-1}$). The effect of the systematic uncertainty on the confidence level is represented by the grey band. The loss due to the systematic uncertainty is rather limited: for a $120\ \mathrm{GeV}/c^2$ Higgs boson, the significance drops from 4.09 to 3.97 for an integrated luminosity of $100\ \mathrm{fb}^{-1}$, and from 7.09 to 6.88 for $300\ \mathrm{fb}^{-1}$.

7 Cross-section measurement

In the case of a Higgs boson discovery, the WH/ZH, H$\rightarrow \gamma\gamma$ channel will be used to measure the cross-section times the branching ratio:

$$\sigma_s \times BR = \frac{N_s}{\epsilon_{sel}\,\mathcal{L}} = \frac{N - N_b^{fit}}{\epsilon_{sel}\,\mathcal{L}} \tag{12}$$

where N_s is the number of signal events given by the difference between the total number N of observed events and the number N_b^{fit} of background events measured by the sideband fit, ϵ_{sel} is the signal selection efficiency and $\mathcal{L}$ the integrated luminosity. The contributions to the total error on the cross-section measurement are the statistical error on the total number of observed events ($\Delta N = \sqrt{N}$), the error on the background estimation with the sideband fit, the error on the measured luminosity and finally the error on the selection efficiency (uncertainty on lepton/photon identification and missing transverse energy, as described in 6.3). The expected precision on the $\sigma \times \mathrm{BR}$ measurement is represented as a function of the integrated luminosity in Figure 35. For a $120\ \mathrm{GeV}/c^2$ Higgs boson, the product of the cross-section and branching ratio will be measured with a precision of 35% after one year of LHC running at high luminosity, and with a precision of 19% after three years of high luminosity running.

8 Results for the Standard Model Higgs Boson

Figure 37 represents the expected statistical significance of the WH/ZH, H$\rightarrow \gamma\gamma$ channel, as a function of m_{H} for three luminosity scenarios, and Figure 38 represents the integrated luminosity required to reach a given statistical significance as a function of m_{H}. The shaded bands correspond to 1σ systematic uncertainty. One year of high luminosity running should allow an observation at 3σ of the SM Higgs boson from the LEP lower limit of $114.4\ \mathrm{GeV}/c^2$ up to $146\ \mathrm{GeV}/c^2$, and three years of running at high luminosity should allow a 5σ discovery from the LEP lower limit up to $148\ \mathrm{GeV}/c^2$.

9 MSSM Interpretation

In the minimal supersymmetric extension of the supermodel (MSSM), two isospin Higgs doublets have to be introduced in order to preserve supersymmetry. The electroweak symmetry-breaking mechanism leads to the existence of five Higgs particles: two CP-even neutral particle (the lightest one is written h and the heaviest one, H), one CP-odd neutral particle A, and two charged particles $\mathrm{H}^{\pm}$. The MSSM Higgs sector is entirely defined by two parameters, here chosen as m_{A}, the mass of the pseudoscalar Higgs particle and $\tan\beta = v2/v1$, the ratio of the vacuum expectation values of the two Higgs doublets.

Within the context of the MSSM, gluon fusion production may be strongly suppressed. The top loop contribution to $gg \rightarrow \mathrm{h}$ may be partially cancelled by the stop loop, when the stop mass is small, *i.e.* for large mixing angle in the stop sector, whereas the partial width $\Gamma(\mathrm{h} \rightarrow \gamma\gamma)$ is dominated by the W boson loop which cannot be cancelled more than 10% by chargino loops for Higgs boson masses greater than $100\ \mathrm{GeV}/c^2$ [8]. For a stop mass of $200\ \mathrm{GeV}/c^2$, the $gg \rightarrow \gamma\gamma$ process may be so heavily suppressed that it would preclude a discovery if m_{A} is below $500\ \mathrm{GeV}/c^2$ [42]. In the MSSM gluophobic scenario, described in [43], the suppression of the $gg \rightarrow \mathrm{h} \rightarrow \gamma\gamma$ process is maximum for m_{A} below $200\ \mathrm{GeV}/c^2$, nearly independantly of $\tan\beta$.

The thresholds for 95% CL, 3σ and 5σ sensitivity of the presented analysis are shown in Figure 39 as a function of m_{h}. After three years of LHC running at high luminosity (integrated luminosity of $300\ \mathrm{fb}^{-1}$), for a Higgs boson mass $m_{\mathrm{h}} = 90\ \mathrm{GeV}/c^2$, the $\mathrm{Wh} \rightarrow \mathrm{l}\nu\gamma\gamma$ process could be discovered with a 5σ significance if its cross-section is greater than 0.48 fb. For a Higgs boson mass $m_{\mathrm{h}} = 115\ \mathrm{GeV}/c^2$, the cross-section has to be greater than 0.57 fb.

The expected cross-section for the $\mathrm{Wh} \rightarrow \mathrm{l}\nu\gamma\gamma$ process is represented in Figure 40, as a function of m_{A} and $\tan\beta$ for the "no mixing" and "maximal mixing" scenarios. In the context of the "maximal mixing" scenario,

it was shown that the gluon fusion production channel $gg \rightarrow \mathrm{h} \rightarrow \gamma\gamma$ may be strongly suppressed for low m_{A} values (typically $m_{\mathrm{A}} \sim 200\ \mathrm{GeV}/c^2$). In this kinematical region, the expected $\mathrm{Wh} \rightarrow \mathrm{l}\nu\gamma\gamma$ cross-section ranges from 0.5 to 0.6 fb. After three years of LHC running at high luminosity, the 5σ sensitivity of the analysis to the $\mathrm{Wh} \rightarrow \mathrm{l}\nu\gamma\gamma$ signal ranges from 0.48 fb to 0.57 fb in the $90 < m_{\mathrm{h}} < 130\ \mathrm{GeV}/c^2$ range.

Therefore, the cross-section sensitivity of the analysis seems to be sufficient to help in covering the MSSM parameter space in case of a "gluophobic" scenario, but it remains to be confirmed with a detailed study based on a full scan of the MSSM parameter space.

10 Conclusion

The possibility to discover a Higgs boson produced in association with a W or Z boson and decaying into two photons has been studied with the CMS full simulation and detector response, including pile-up consistent with the LHC high luminosity operation ($\mathcal{L} = 10^{34}\ \mathrm{cm}^{-2}\mathrm{s}^{-1}$). Both signal and background uncertainties have been included.

Particular care has been taken with the analysis method, in order to be able to fully exploit real data once they become available. In this way an integrated luminosity of $5\ \mathrm{fb}^{-1}$ should be sufficient to optimise the likelihood method which permits the rejection of multijet backgrounds ($\mathrm{b\overline{b}}$, γ-jet and $\mathrm{t\overline{t}}$ processes). The utilisation of simulated data for these backgrounds thus would become irrelevant. Besides, final background rates could be measured with real data in kinematic regions where there is no signal. This will permit a considerable simplification of the estimation of systematic errors on these background rates. With an integrated luminosity of $100\ \mathrm{fb}^{-1}$, the error on the backround rate measurement should reach 11% in the case of an analysis optimised for a Higgs boson having a mass of $120\ \mathrm{GeV}/c^2$. On the other hand, the selection method fully relies upon the utilisation of simulated data for the signal, and thus suffers from the effects of systematic errors on it. However, the statistical method, developed by the LEP Higgs working group, allows to avoid this constraint: no significant dependence of the discovery potential as a function of the uncertainty on the signal is observed.

The conclusion of this work indicates that after three years of LHC running at high luminosity, it is expected that the SM Higgs boson can be discovered in this channel with 5σ significance between the $114.4\ \mathrm{GeV}/c^2$ LEP lower limit and $148\ \mathrm{GeV}/c^2$. For heavier Higgs boson masses, the preferred search channels are the $\mathrm{p} + \mathrm{p} \rightarrow \mathrm{H} \rightarrow \mathrm{ZZ}^*$ and $\mathrm{p} + \mathrm{p} \rightarrow \mathrm{H} \rightarrow \mathrm{WW}^*$ processes, which are abundantly produced and give clean signatures, especially when the final state involves muons and/or electrons [39, 44].

11 Acknowledgements

The authors would like to express their thanks to R. Barbier, D. Denegri, M. Dubinin, S. Lowette, L. Malgeri and S. Nikitenko for their help, advice and constructive remarks.

References

[1] CMS Collaboration, *"The Compact Muon Solenoid - Technical Proposal"*, **CERN/LHCC 94/38**.

[2] LEP Electroweak working group and Tevatron Electroweak working group, *"Precision tests of the Standard Model"*, presented by C. Parkes at the XXIII International Conference on High Energy Physics, Moscow, 26 July 2006;
The LEP Electroweak working group, **http://lepewwg.web.cern.ch/LEPEWWG**.

[3] S.Ambrosanio *et al.*, *"Implications of the Higgs Boson Searches on Different Soft SUSY-breaking Scenarios"*, Nucl. Phys. B **624**, 3 (2002).

[4] R. Barate *et al.*, LEP Working Group for Higgs boson searches, *"Search for the standard model Higgs boson at LEP"*, Phys. Lett. B **565**, 61 (2003).

[5] LEP Working Group for Higgs boson searches, *"Search for neutral MSSM Higgs bosons at LEP"*, Eur. Phys. J. C **47**, 547 (2006).

[6] M. Pieri *et al.*, *"Inclusive search for the Higgs Boson in the* $\mathrm{H} \rightarrow \gamma\gamma$ *channel"*, **CMS Note 2006/112**.

[7] C. Seez and T.S. Virdee, *"Using Tracks to Locate the two Photon Vertex"*, **CMS Note 1993/092**;
C. Seez, *"An Algorithm Using Tracks to Locate the two Photon Vertex"*, **CMS Note 1993/115**;
D.J. Graham, *"An algorithm using tracks to locate the two photon vertex at high luminosity"*, **CMS Note 1995/115**.

[8] A. Djouadi, *"Squark effects on Higgs boson production and decay at the LHC"*, PM/98-06, **[arXiv:hep-ph/9806315]**;
A. Djouadi, Phys. Lett. B **435** (1998) 101;
A. Djouadi *et al.*, *"The coupling of the lightest SUSY Higgs on two photons in the decoupling regime"*, Eur. Phys. J. **C 1** (1998) 149.

[9] J.L. Agram *et al.*, *"Associated* $\mathrm{t\bar{t}H}$ *production with* $\mathrm{H} \rightarrow \gamma\gamma$ *in CMS"*, CMS Note in preparation.

[10] M. Dubinin *"Higgs Boson Signal in the reactions* $\mathrm{pp} \rightarrow \gamma\gamma + 2$ *forward jets"*, **CMS Note 2001/022**;
M. Dubinin *et al.*, *"The vector boson fusion production with* $\mathrm{H} \rightarrow \gamma\gamma$*"*, **CMS Note 2006/097**.

[11] M. Dubinin *et al.*, *"Light Higgs Boson Signal at LHC in the reaction* $\mathrm{pp} \rightarrow \gamma\gamma$*+jet and* $\mathrm{pp} \rightarrow \gamma\gamma$*+lepton"*, **CMS Note 1997/101**.

[12] R. Kinnunen and D. Denegri *"Expected SM/SUSY Higgs Observability in CMS"*, **CMS Note 1997/057**.

[13] Guillaume Eynard, Ph.D. Thesis, *"Etude de la production associée du boson de Higgs* $\mathrm{HW}, \mathrm{Ht\bar{t}}, \mathrm{HZ} \rightarrow \gamma\gamma + \mathrm{e}^{\pm}/\mu^{\pm} + \mathrm{X}$ *avec le détecteur ATLAS, auprès du LHC"*, Université Joseph Fourier (1998).

[14] P.-H Beauchemin and G. Azuelos, *"Search for the Standard Model Higgs Boson in the* $\gamma\gamma + E_T^{miss}$ *channel"*, **ATL-PHYS-2004-028**.

[15] Olivier Ravat, Ph.D. Thesis, *"Etude du Calorimètre électromagnétique de l'expérience CMS et recherche de bosons de Higgs neutres dans le canal de production associée"*, **LYCEN-T2004-29**.

[16] E. Boos *et al.*, Nucl. Instr. Meth. **A534** (2004) 250, **[arXiv:hep-ph/0403113]**;
A. Pukhov *et al.*, INP report INP-MSU-98-41-542, **[arXiv:hep-ph/9908288]**.

[17] M. Spira, *"QCD Effects in Higgs Physics"*, Fortsch. Phys. **46** (1998) 203-284, **[arXiv:hep-ph/9705337]**;
T. Han and S. Willenbrock, Phys. Lett. **B273** (1991) 167.

[18] A. Djouadi, J. Kalinowski and M. Spira, *"HDECAY: A program for Higgs Boson Decays in the Standard Model and its Supersymmetric Extension"*, Comput. Phys. Commun. **108** (1998) 56, **[arXiv:hep-ph/9704448]**.

[19] T. Sjostrand, Comput. Phys Commun. **80** (1994) 74;
S. Mrenna, Comput. Phys Commun. **101** (1997) 292;
T. Sjostrand *et al.*, Comput. Phys Commun. **135** (2001) 238, **[arXiv:hep-ph/0010017]**;
T. Sjostrand, L. Lonnblas, S. Mrenna and P. Skands, **[arXiv:hep-ph/0308153]**.

[20] M. Beneke *et al.*, *"Top quark physics"*, **[arXiv:hep-ph/0003033]**;
F. Maltoni, *"Theoretical Issues and Aims at the Tevatron and LHC"*, Hadron Collider Physics Symposium, Les Diablerets, 4-9 July 2005.

[21] Geant 3, CERN Program Library Long Writeup W5013.

[22] CMS Collaboration, *"The Tridas Project Design Report, Volume 1: The Trigger Systems"*, **CERN/LHCC 2000/038**, **CMS TDR 6.1**.

[23] CMS Collaboration, *"The Tridas Project Design Report, Volume 2: Data acquisition and High-Level Trigger"*, **CERN/LHCC 2002/002**, **CMS TDR 6.2**.

[24] J. D'Hondt *et al.*, *"Electron and muon reconstruction in single leptonic* $\mathrm{t\bar{t}}$ *events"*, **CMS Note 2006/024**.

[25] CMS Collaboration, *"Physics Technical Design Report, Volume 1: Detector Performance and Software"*, **CERN/LHCC 2006/001**, (2006) 375.

[26] V. Litvin *et al.*, *"The rejection of background to the* $\mathrm{H} \to \gamma\gamma$ *process using isolation criteria based on information from electromagnetic calorimeter and tracker"*, **CMS Note 2002/030**.

[27] M. Pieri *et al.*, *"Distinguishing Isolated Photons from Jets"*, **CMS Note 2006/007**.

[28] E. Meschi *et al.*, *"Electron reconstruction in the CMS Electromagnetic Calorimeter"*, **CMS Note 2001/034**.

[29] ORCA, Object Oriented Reconstruction for CMS Analysis, **http://cmsdoc.cern.ch/orca**.

[30] CMS Collaboration, *"Physics Technical Design Report, Volume 1: Detector Performance and Software"*, **CERN/LHCC 2006/001**, (2006) 390.

[31] CMS Collaboration, *"Physics Technical Design Report, Volume 1: Detector Performance and Software"*, **CERN/LHCC 2006/001**, (2006) 332.

[32] CMS Collaboration, *"Physics Technical Design Report, Volume 1: Detector Performance and Software"*, **CERN/LHCC 2006/001**, (2006) 349.

[33] CMS Collaboration, *"Physics Technical Design Report, Volume 1: Detector Performance and Software"*, **CERN/LHCC 2006/001**, (2006) 407.

[34] The LEP Higgs Working Group, **http://lephiggs.web.cern.ch/LEPHIGGS/www/Welcome.html**;
A.L. Read, *"Presentation of search results: the* CL_s *technique"*, Journal of Physics G: Nucl. Part. Phys. **28** (2002) 2693;
A.L. Read, *"Modified Frequentist Analysis of Search Results (The CLs Method)"*, **CERN 2000-005**;
T. Junk,*"Confidence level computation for combining searches with small statistics"*, NIM **A434** (1999) 435.

[35] R.D. Cousins and V.L. Highland, *"Incorporating systematic uncertainties into an upper limit"*, NIM **A320** (1992) 331.

[36] The CTEQ collaboration, J. Pumplin *et al.*, *"New Generation of Parton Distributions with Uncertainties from Global QCD Analysis"*, JHEP 0207 (2002) 12, **[arXiv:hep-ph/0201195]**.

[37] A. Djouadi and S. Ferrag, *"PDF Uncertainties in Higgs Production at Hadron Colliders"*, **[arXiv:hep-ph/0310209]**.

[38] CMS Collaboration, *"Physics Technical Design Report, Volume 1: Detector Performance and Software"*, **CERN/LHCC 2006/001**, (2006) 315;
CMS Collaboration, *"Physics Technical Design Report, Volume 2: Physics Performance"*, **CERN/LHCC 2006/021**, (2006) 532.

[39] S. Baffioni *et al.*, *"Discovery potential for the SM Higgs boson in the* $\mathrm{H} \to \mathrm{ZZ} \to \mathrm{e^+e^-e^+e^-}$ *decay channel"*, **CMS Note 2006/115**.

[40] CMS Collaboration, *"Physics Technical Design Report, Volume 2: Physics Performance"*, **CERN/LHCC 2006/021**, (2006) 532.

[41] CMS Collaboration, *"Physics Technical Design Report, Volume 2: Physics Performance"*, **CERN/LHCC 2006/021**, (2006) 533.

[42] R. Kinnunen, S. Lehti, A. Nikitenko, S. Rantala, *"Effects of large mixing and light stop for* $\mathrm{h} \to \gamma\gamma$ *in MSSM"*, **CMS Note 2000/043**.

[43] CMS Collaboration, *"Physics Technical Design Report, Volume 2: Physics Performance"*, **CERN/LHCC 2006/021**, (2006) 384.

[44] G.Davatz *et al., "Standard Model Higgs discovery potential of CMS in* $\mathrm{H} \to \mathrm{WW} \to \ell\nu\ell\nu$ *channel"*, **CMS Note 2006/047**;
F. Beaudette *et al., "Search for a light Standard Model Higgs model in the* $\mathrm{H} \to \mathrm{WW}^* \to \mathrm{e}\nu\mathrm{e}\nu$ *channel*, **CMS Note 2006/114**;
H. Pi *et al., "Search for Standard Model Higgs boson via vector boson fusion in the* $\mathrm{H} \to \mathrm{WW} \to \ell\nu\mathrm{jj}$ *channel with* $120 < m_{\mathrm{H}} < 250\ \mathrm{GeV}/c^2$*"*, **CMS Note 2006/092**;
S.Abdullin *et al., "Search strategy for the Standard Model Higgs boson in the* $\mathrm{H} \to \mathrm{ZZ} \to 4\mu$ *decay channel using M(4*μ*)-dependent cuts"*, **CMS Note 2006/122**;
M. Aldaya *et al., "Discovery potential and search strategy for the Standard Model Higgs boson in the* $\mathrm{H} \to \mathrm{ZZ}^{(*)} \to 4\mu$ *decay channel using a mass-independent analysis"*, **CMS Note 2006/106**;

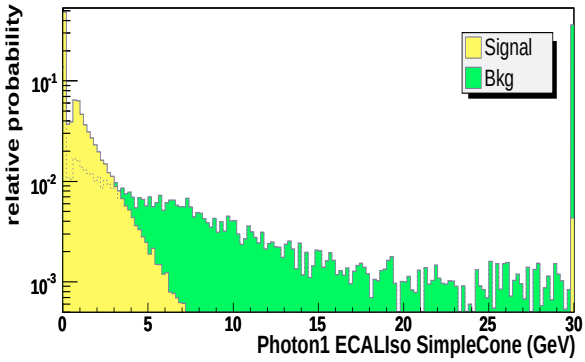

Figure 1: Sum of the transverse energy of island basic clusters with $\Delta R < 0.3$ from the highest $\mathrm{E_T}$ photon, excluding basic clusters belonging to the photon supercluster at the preselection level.

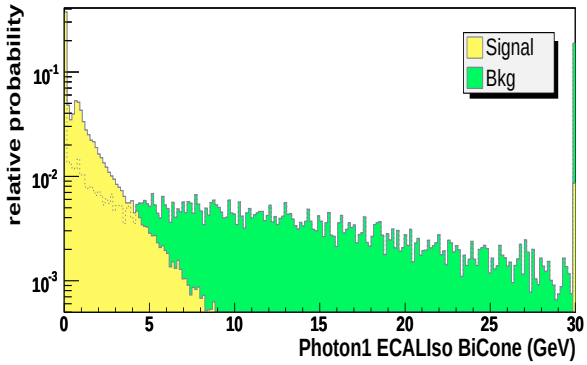

Figure 2: Sum of the transverse energy of island basic clusters with $0.08 < \Delta R < 0.3$ from the highest $\mathrm{E_T}$ photon at the preselection level.

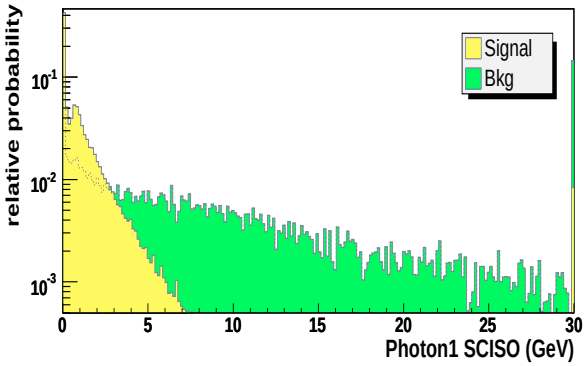

Figure 3: Sum of the transverse energy of island basic clusters with $0.08 < \Delta R < 0.35$ from the highest $\mathrm{E_T}$ photon, excluding basic clusters in a $|\Delta\eta| < 0.03$ ring at the preselection level.

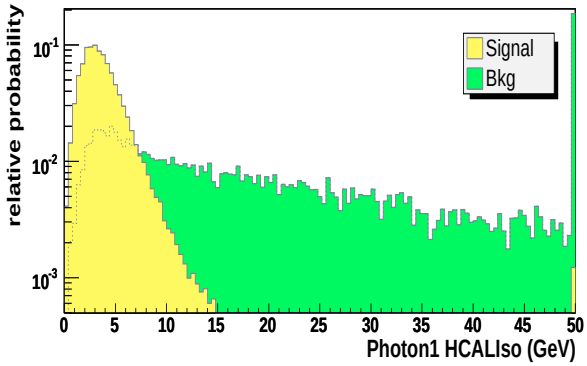

Figure 4: Sum of the transverse energy of the HCAL towers with $\Delta R < 0.3$ from the highest $\mathrm{E_T}$ photon at the preselection level.

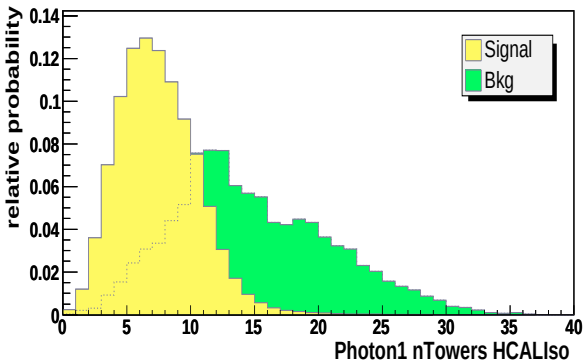

Figure 5: Number of HCAL towers hit within a cone $\Delta R < 0.3$ around the highest $\mathrm{E_T}$ photon at the preselection level.

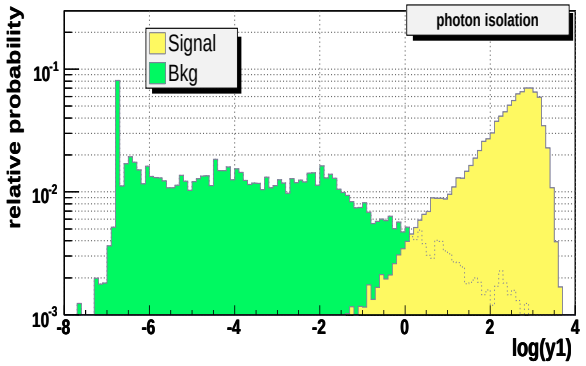

Figure 6: Combined likelihood variable used in photon isolation. The cut $\log(y_1) > -0.4$ is applied in the analysis.

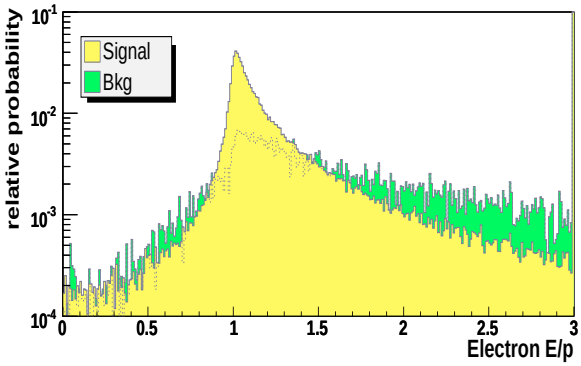

Figure 7: Ratio of the electron calorimeter energy over its tracker momentum at the preselection level.

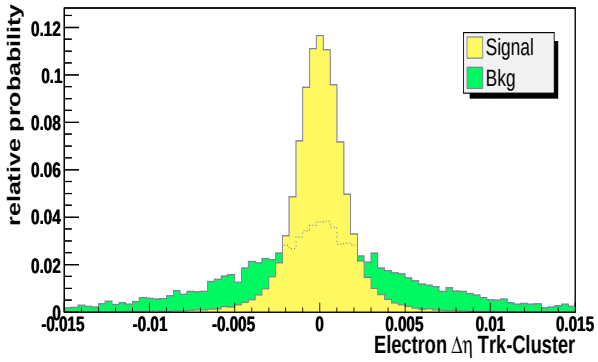

Figure 8: $\Delta\eta$ between the electron track and its matching supercluster at the preselection level.

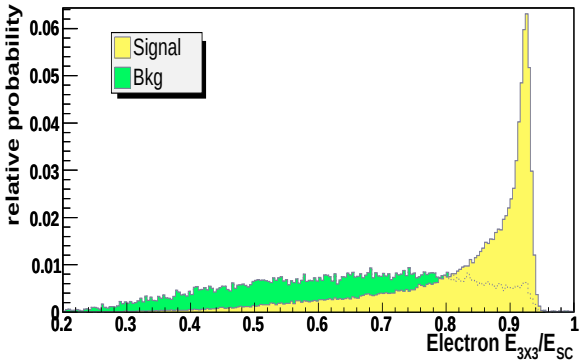

Figure 9: Ratio of the energy sum of 3×3 crystals over supercluster energy at the preselection level.

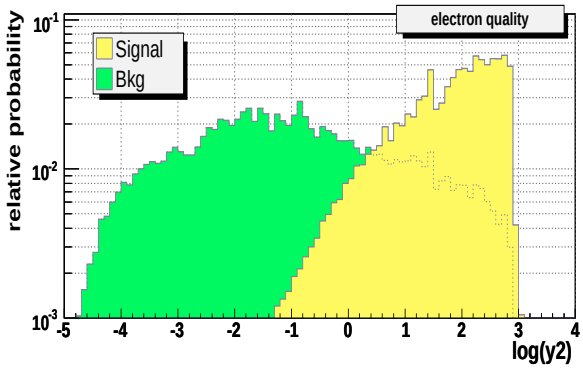

Figure 10: Distribution of the combined likelihood variable reflecting the quality of the electron reconstruction. The cut $\log(y_2) > -0.6$ is applied in the analysis.

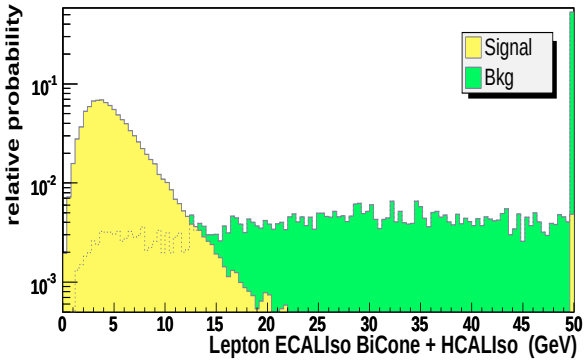

Figure 11: Sum of the transverse energy of island basic clusters in a cone $0.08 < \Delta R < 0.3$ around the lepton, added to the sum of the transverse energy of the HCAL towers in a cone $\Delta R < 0.3$ around the lepton. The distributions are shown at the preselection level.

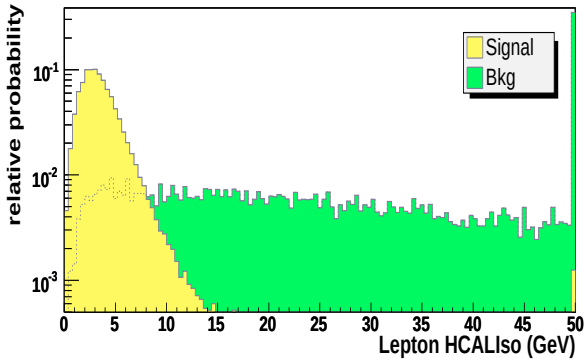

Figure 12: Sum of the transverse energy of the HCAL towers in a cone $\Delta R < 0.3$ around the lepton at the preselection level.

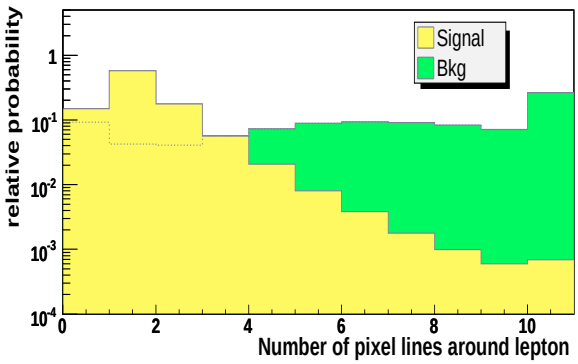

Figure 13: Number of pixel lines in a cone $\Delta R < 0.3$ around the lepton at the preselection level.

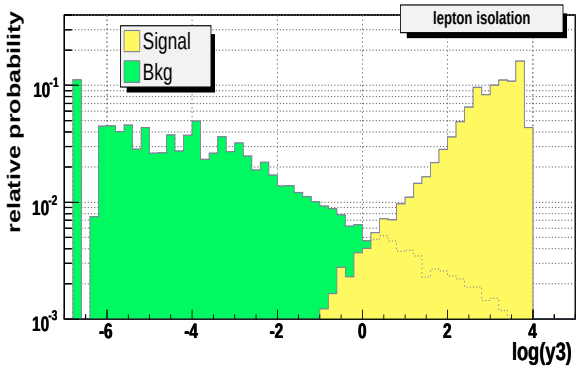

Figure 14: Distribution of the combined variable used for lepton isolation. The cut $\log(y_3) > -0.3$ is applied in the analysis. The discontinuities observed on the distributions are due to the use of a discrete variable (the number of pixel lines around the lepton) in the likelihood.

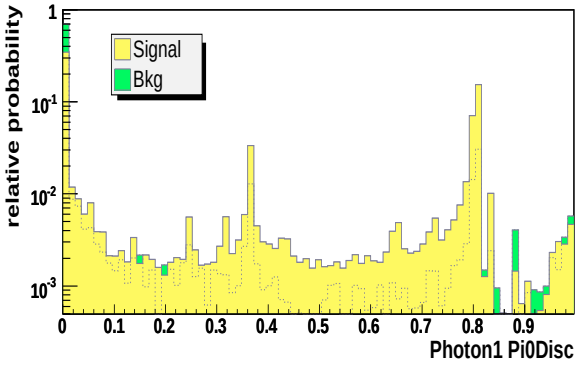

Figure 15: Output of the standard ORCA π^0 discriminator applied to the first photon at the preselection level.

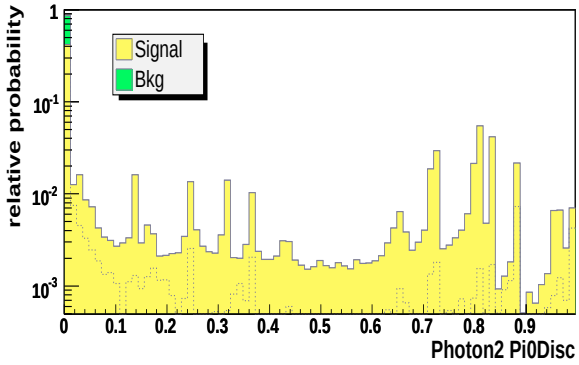

Figure 16: Output of the standard ORCA π^0 discriminator applied to the second photon at the preselection level.

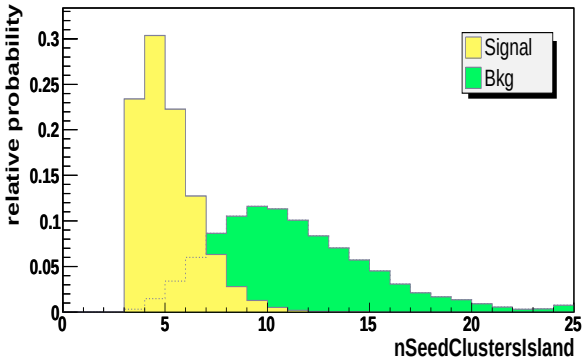

Figure 17: Number of seed clusters reconstructed with the Island algorithm at the preselection level.

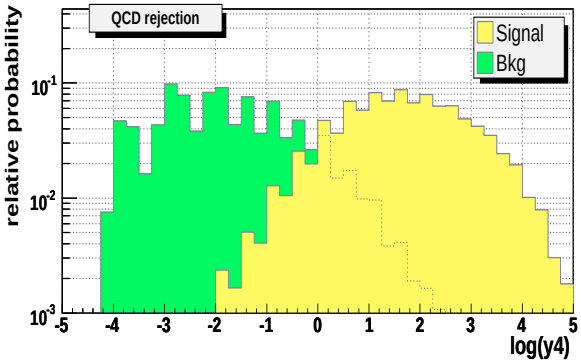

Figure 18: Distribution of the combined variable used to reject multijet events. The discontinuities observed on the distributions are due to the use of discrete variables in the likelihood. The cut $\log(y_4) > -0.8$ is applied in the analysis.

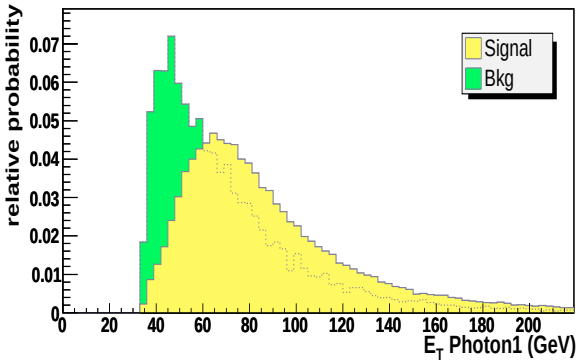

Figure 19: Transverse energy of the highest $\mathrm{E_T}$ photon before the final likelihood selection.

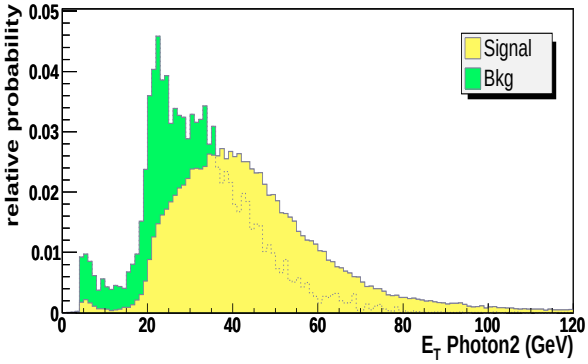

Figure 20: Transverse energy of the second highest $\mathrm{E_T}$ photon before the final likelihood selection.

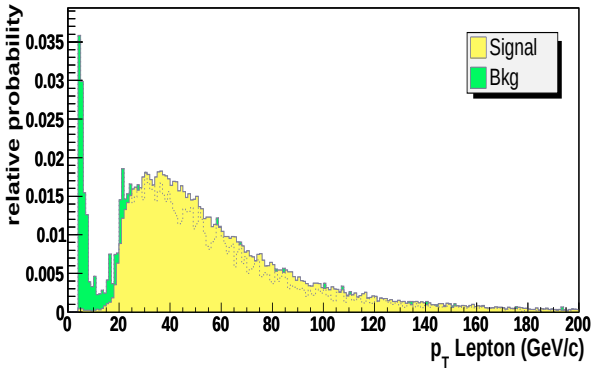

Figure 21: Transverse energy of the selected lepton before the final likelihood selection.

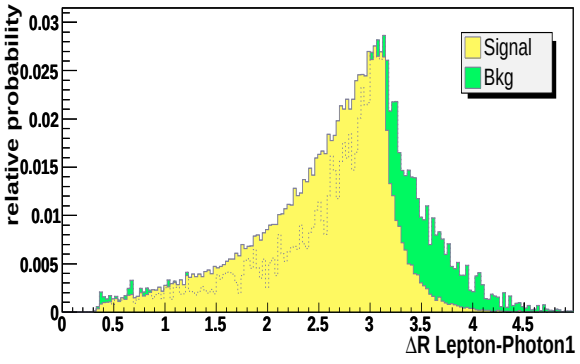

Figure 22: ΔR distance between the lepton and the highest $\mathrm{E_T}$ photon before the final likelihood selection.

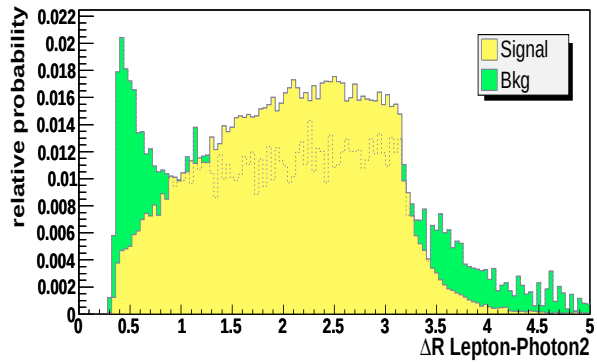

Figure 23: ΔR distance between the lepton and the second highest E_T photon before the final likelihood selection.

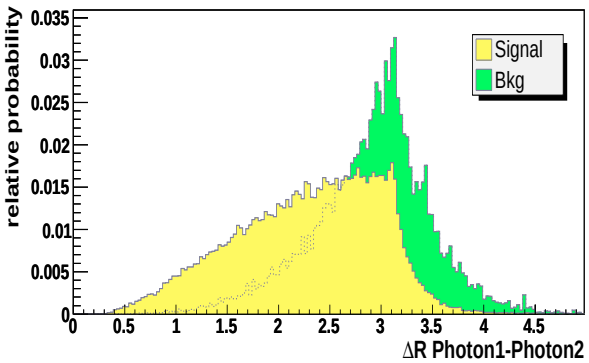

Figure 24: ΔR distance between the two photons before the final likelihood selection.

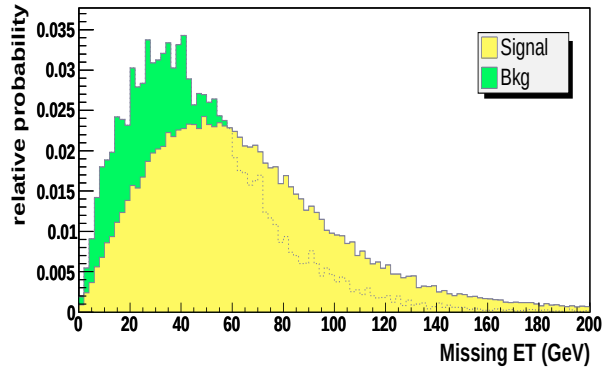

Figure 25: Missing transverse energy before the final likelihood selection.

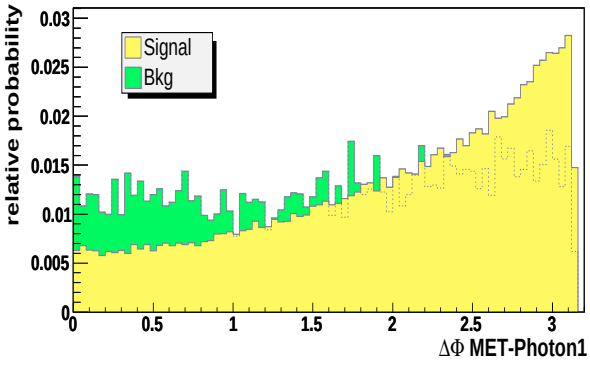

Figure 26: $\Delta\Phi$ between missing energy direction and highest E_T photon before the final likelihood selection.

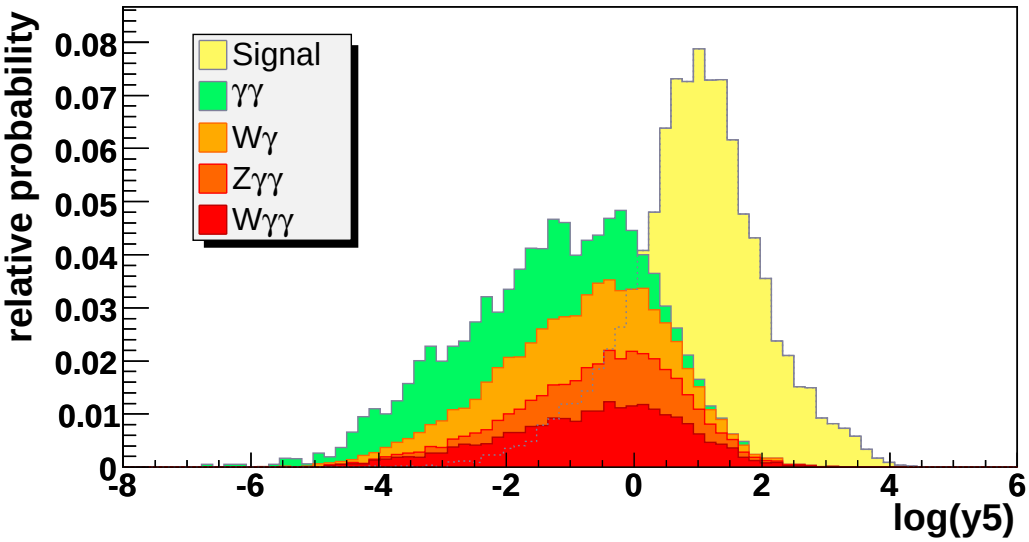

Figure 27: Distribution of the kinematical combined variable y_5 for the signal ($m_H = 120$ GeV/c^2) and for the background. The optimal working point is obtained with a cut $log(y_5) > 0.35$.

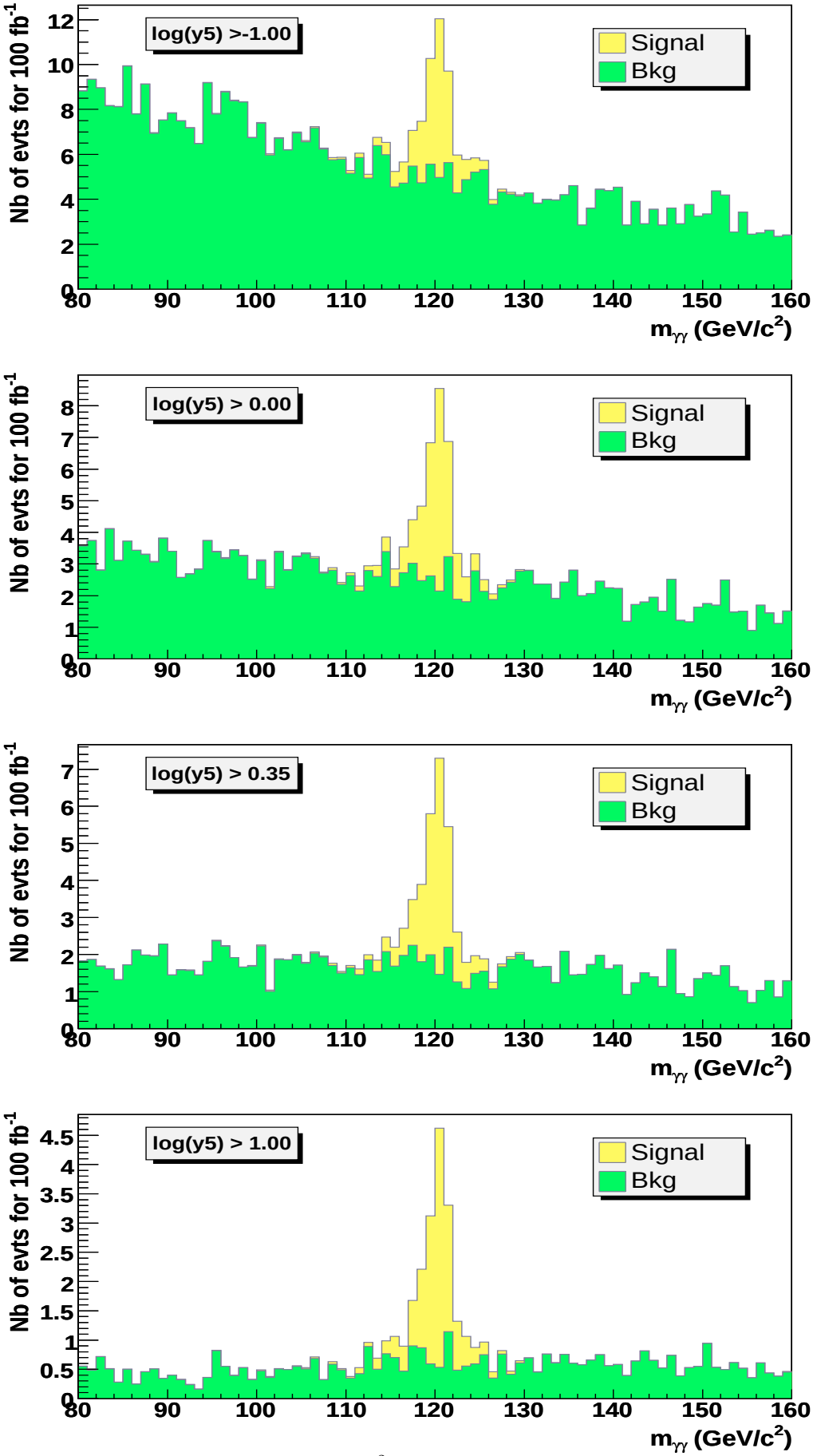

Figure 28: Reconstructed $\gamma\gamma$ mass for a 120 GeV/c^2 Higgs boson signal (light grey) and for backgroud (dark grey) after different cuts on the final likelihood ouput variable y_5.

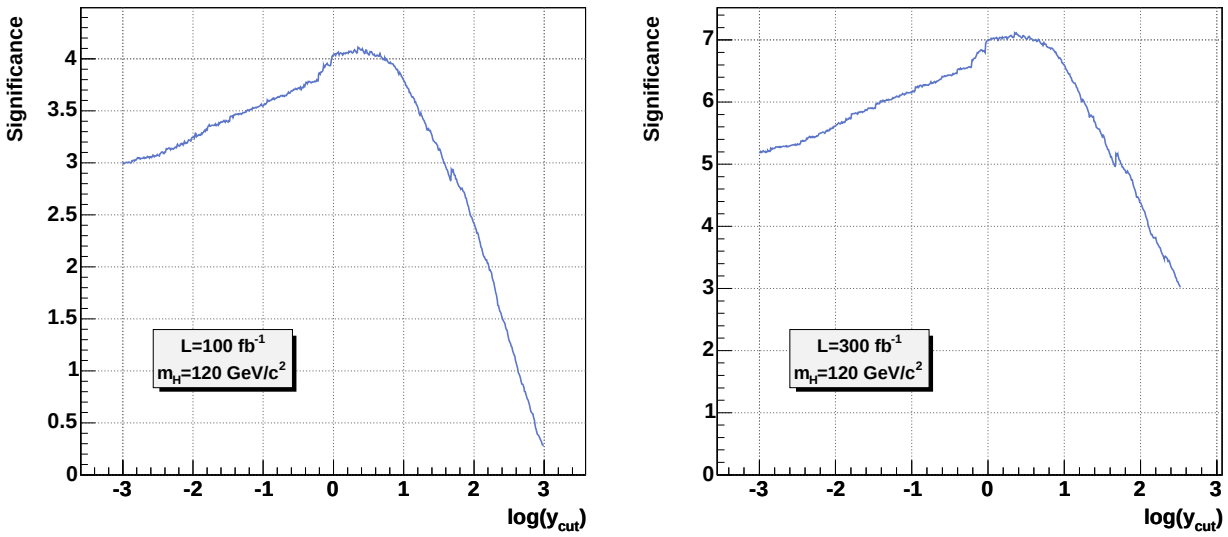

Figure 29: Statistical significance in units of σ as a function of the cut on the final combined variable $\log(y_5)$, for $m_{\mathrm{H}} = 120\ \mathrm{GeV}/c^2$ and for integrated luminosities of $100\ \mathrm{fb}^{-1}$ (left) and $300\ \mathrm{fb}^{-1}$ (right).

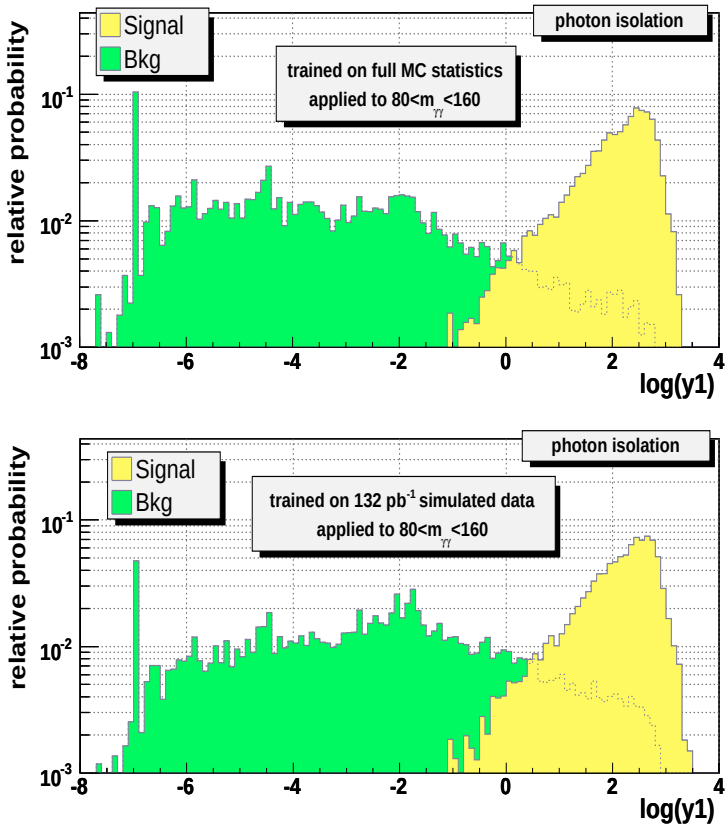

Figure 30: Distribution of the photon isolation combined variable y_1 obtained by the standard analysis using the full MC statistics (top) and obtained by optimizing the likelihood with a sample of 132 fb^{-1} of simulated data corresponding to possible future real dataset taken in the $20 < m_{\gamma\gamma} < 80\ \mathrm{GeV}/c^2$ sideband (bottom). In this last case, the increase of the background tail in the signal region is mainly due to γ-jet and $\mathrm{t\bar{t}}$ events.

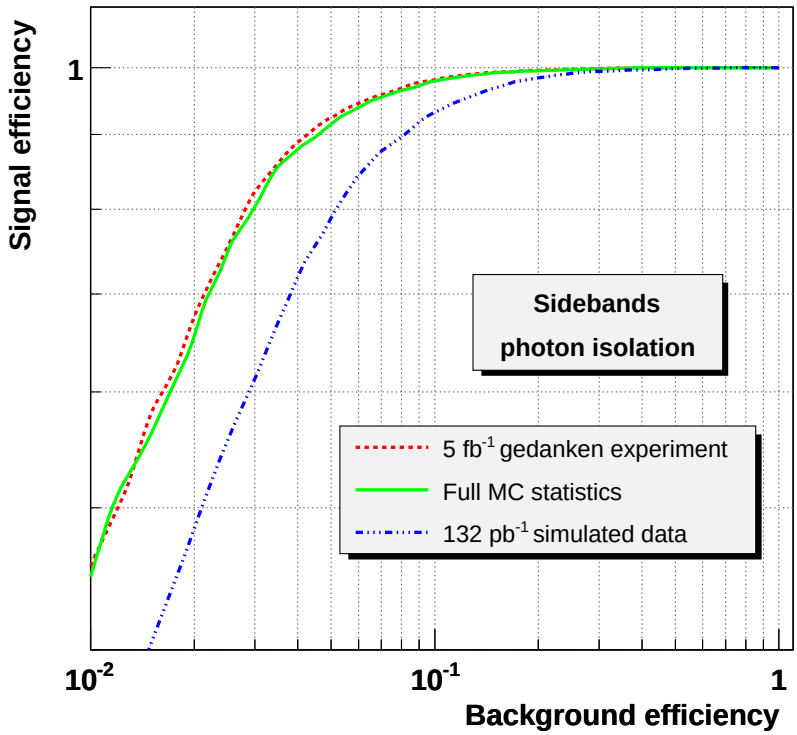

Figure 31: Comparison of the performance obtained by the standard analysis using the full MC statistics (solid line) with the performance obtained when optimizing the photon isolation likelihood with a sample of 132 fb^{-1} of simulated data corresponding to possible future real dataset taken in the $20 < m_{\gamma\gamma} < 80$ GeV$/c^2$ sideband (dash-dotted line), as explained in the text. To increase the available statistics in the sideband, gedanken experiments were generated for an equivalent luminosity of 5 fb^{-1}. The results of the optimization on these sideband events is represented by the dotted line.

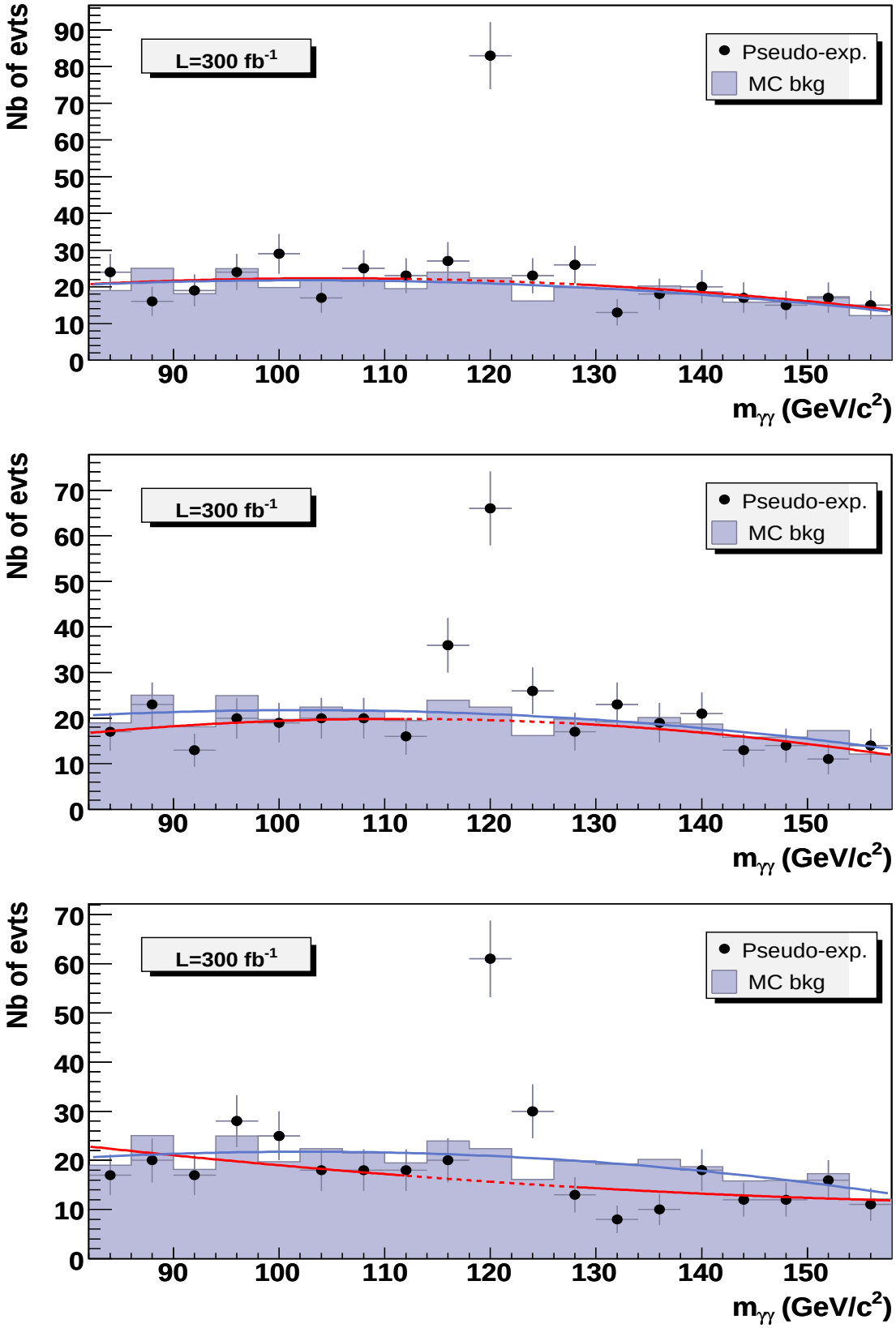

Figure 32: Background measurement in the signal region with a fit on the $m_{\gamma\gamma}$ sideband. The fit of the full MC statistics over the whole mass range is represented by the solid light gray line. The fit for the signal-like pseudo-experiment (dark grey) is performed on the sidebands, *i.e.* after the exclusion of the signal window represented by the dotted line. The number of background events in the signal region is given by the integral of the fit function in this window. Three pseudo-experiments are represented for an integrated luminosity of 300 fb^{-1} and a 120 GeV/c^2 Higgs boson mass hypothesis: one gives a good accuracy of the background estimation (2.9%, top plot), one a typical precision (6.9%, middle plot) and the last a poor estimation (17.1%, bottom plot).

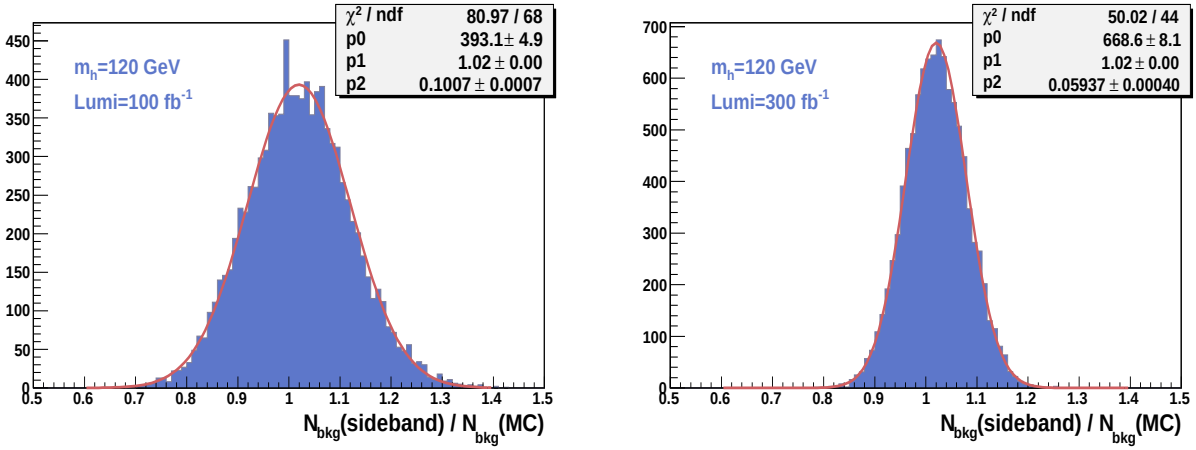

Figure 33: Ratio between the number of background events in the signal region estimated by the fit of the sideband data for the generated pseudo-experiments and the number of expected background events given by the full statistics MC for $m_{\mathrm{H}} = 120\ \mathrm{GeV}/c^2$ and integrated luminosities of $100\ \mathrm{fb}^{-1}$ (left) and $300\ \mathrm{fb}^{-1}$ (right).

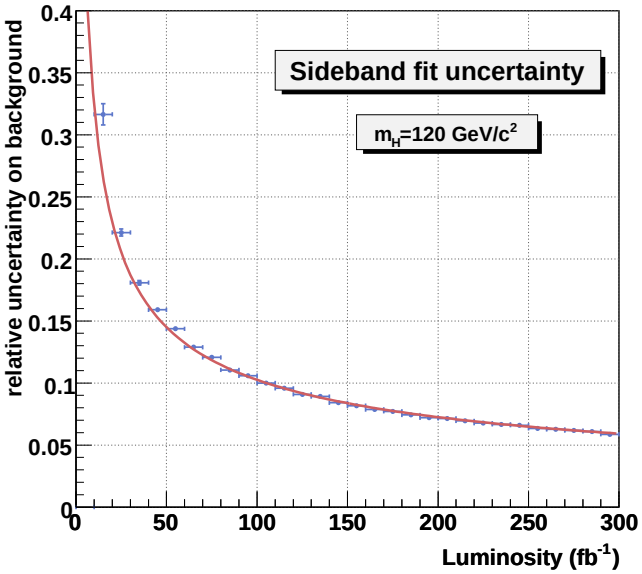

Figure 34: Relative uncertainty on the background estimation by the sideband fit method as a function of the integrated luminosity with LHC running at high luminosity for a Higgs boson mass of $120\ \mathrm{GeV}/c^2$.

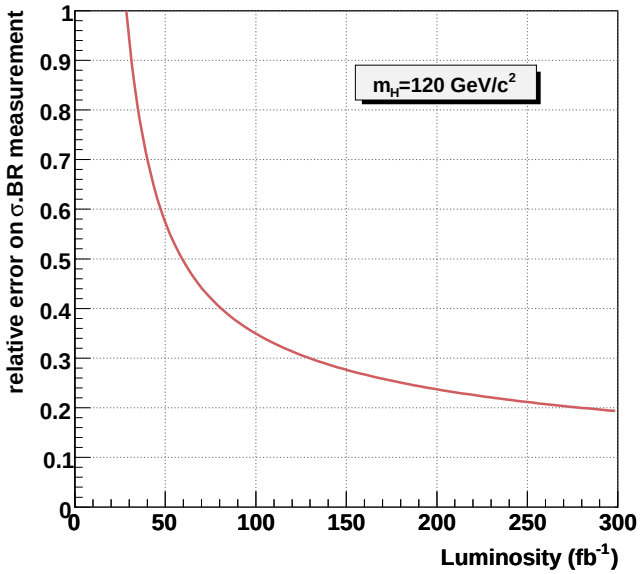

Figure 35: Precision on the measurement of the product of cross-section and branching ratio as a function of the integrated luminosity with LHC running at high luminosity for a $120\ \mathrm{GeV}/c^2$ Higgs boson.

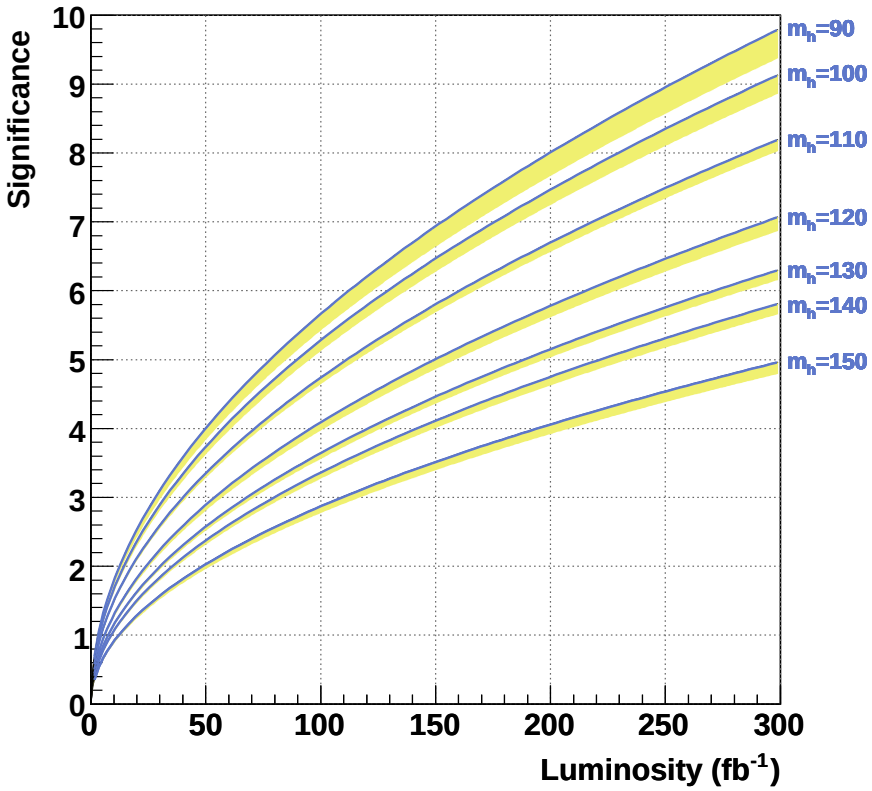

Figure 36: Statistical significance for different Higgs boson mass hypotheses as a function of the integrated luminosity with LHC running at high luminosity. The 1σ systematic uncertainty is represented by the grey band.

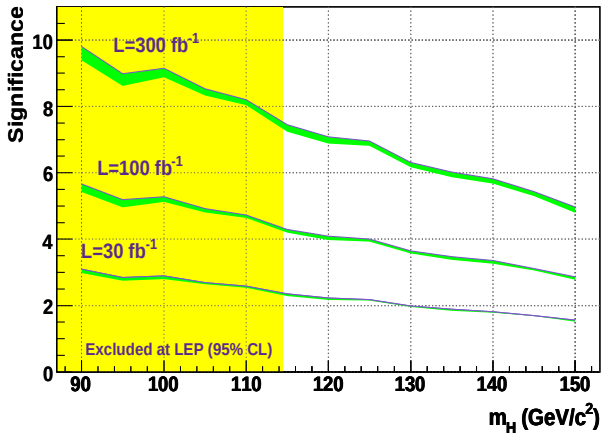

Figure 37: Statistical significance as a function of m_{H} after 30 fb^{-1}, 1 year and 3 year of high luminosity running. The 1σ systematic uncertainty is represented by the grey band.

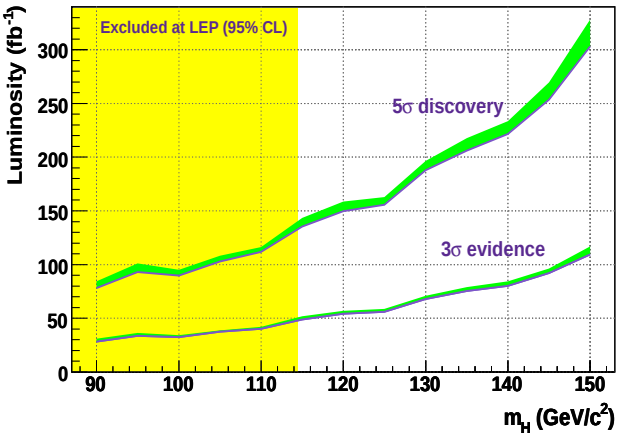

Figure 38: Integrated luminosity needed for a 5σ discovery, and for a 3σ observation as a function of m_{H}. The 1σ systematic uncertainty is represented by the grey band.

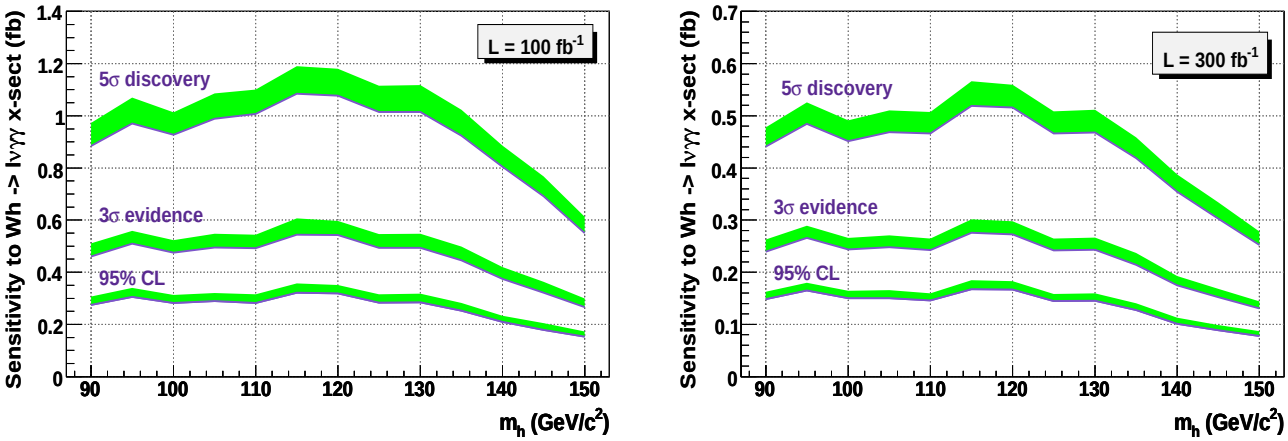

Figure 39: Analysis sensitivity to the $\mathrm{Wh} \rightarrow \mathrm{l}\nu\gamma\gamma$ cross-section as a function of m_{h} after one year (left) and three years (right) of high luminosity runnning. The 1σ systematic uncertainty is represented by the grey band.

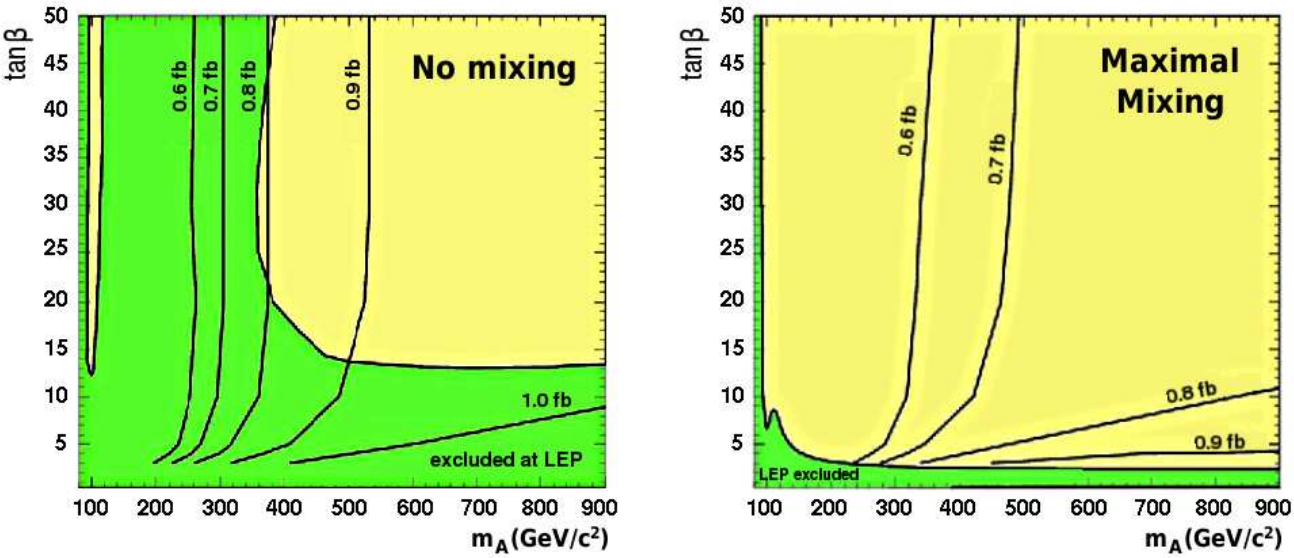

Figure 40: Expected cross-sections for $\mathrm{WH} \rightarrow \mathrm{l}\nu\gamma\gamma$ as a function of m_{A} and tan β in the no mixing scenario (left) and in the maximal mixing scenario (right) of the MSSM.